Gas phase Elemental abundances in Molecular cloudS (GEMS). I. The prototypical dark cloud TMC 1

Fuente, A.; Navarro, D.G.; Caselli, P.; Gerin, M.; Kramer, C.; Roueff, E.; ... ; Ballester, M.Y.

Astronomy & Astrophysics manuscript no. art-TMC1-astroph
September 14, 2018

Gas phase Elemental abundances in Molecular cloudS (GEMS)

I. The prototypical dark cloud TMC 1

A. Fuente[1], D. Navarro[1], P. Caselli[2], M. Gerin[3], C. Krammer[4], E. Roueff[5], V. Wakelam[6], T. Alonso-Albi[1], R. Bachiller[1], S. Cazaux[7], B. Commercon[8], R. Friesen[9], S. García-Burillo[1], B. M. Giuliano[2], J. R. Goicoechea[10], P. Gratier[6], A. Hacar[11], I. Jiménez-Serra[12], J. Kirk[13], V. Lattanzi[2], J. C. Loison[14], P. J. Malinen[15], N. Marcelino[10], R. Martín-Doménech[16], G. Muñoz-Caro[12], J. Pineda[2], M. Tafalla[1], B. Tercero[1], D. Ward-Thompson[17], S. Treviño-Morales[18], P. Riviére-Marichalar[10], O. Roncero[10], and T. Vidal[6]

[1] Observatorio Astronómico Nacional (OAN), Alfonso XII, 3 28014, Madrid, Spain
[2] Centre for Astrochemical Studies, Max-Planck-Institute for Extraterrestrial Physics, Giessenbachstrasse 1, 85748, Garching, Germany
[3] Observatoire de Paris, PSL Research University, CNRS, École Normale Supérieure, Sorbonne Universités, UPMC Univ. Paris 06, 75005, Paris, France
[4] Instituto Radioastronomía Milimétrica (IRAM), Av. Divina Pastora 7, Nucleo Central, 18012, Granada, Spain
[5] LERMA, Observatoire de Paris, PSL Research University, CNRS, UMR8112, Place Janssen, 92190, Meudon Cedex, France
[6] Laboratoire d'astrophysique de Bordeaux, Univ. Bordeaux, CNRS, B18N, allée Geoffroy Saint-Hilaire, 33615, Pessac, France
[7] Faculty of Aerospace Engineering, Delft University of Technology, Delft, The Netherlands ; University of Leiden, P.O. Box 9513, NL, 2300 RA, Leiden, The Netherlands
[8] École Normale Supérieure de Lyon, CRAL, UMR CNRS 5574, Université Lyon I, 46 Allée d'Italie, 69364, Lyon Cedex 07, France
[9] Dunlap Institute for Astronomy & Astrophysics, University of Toronto, 50 St. George Street, Toronto, ON M5S 3H4, Canada 0000-0001-7594-8128
[10] Instituto de Física Fundamental (CSIC), Calle Serrano 121, 28006, Madrid, Spain
[11] Laboratoire d'Astrophysique de Bordeaux, Univ. Bordeaux, CNRS, B18N, Allée Geoffroy Saint-Hilaire, 33615, Pessac, France
[12] Leiden Observatory, Leiden University, PO Box 9513, 2300-RA, Leiden, The Netherlands
[13] Centro de Astrobiología (CSIC-INTA), Ctra. de Ajalvir, km 4, Torrejón de Ardoz, 28850, Madrid, Spain
[14] Department of Physics, University of Warwick, Coventry CV4 7AL, UK
[15] Institut des Sciences Moléculaires (ISM), CNRS, Univ. Bordeaux, 351 cours de la Libération, F-33400, Talence, France
[16] Department of Physics, University of Helsinki, PO Box 64, 00014, Helsinki, Finland; Institute of Physics I, University of Cologne, Cologne, Germany
[17] Harvard-Smithsonian Center for Astrophysics, Cambridge, MA 02138, USA
[18] Jeremiah Horrocks Institute, University of Central Lancashire, Preston PR1 2HE, UK
[19] Chalmers University of Technology, Onsala Space Observatory, 439 92 Onsala, Sweden.

September 14, 2018

ABSTRACT

Context. This is the first paper of the (Gas phase Elemental abundances in Molecular CloudS) project and is dedicated to the study of the prototypical dark cloud TMC 1.
Aims. GEMS is an IRAM 30m Large Programme aimed to determine the S, C, N, O depletions and X(e^-) as a function of visual extinction in a selected set of prototypical star forming regions.
Methods. Extensive millimeter observations have been carried out with the IRAM 30m telescope (3mm and 2mm) and the 40m Yebes telescope (bands K and Q) to determine the fractional abundances of CO, HCO^+, HCN, CS, SO, HCS^+ and N_2H^+ in three cuts across the TMC 1 filament. These cuts intersect the dense filament at the well-known positions TMC 1-CP, TMC 1-NH3 and TMC 1-C and cover a visual extinction range of ~ 3 mag to >20 mag. We determine the S, C, N, O depletions and X(e^-) through the comparison of our molecular abundance estimates with the Meudon PDR code.
Results. Two phases with differentiated physical conditions and chemistry can be distinguished in TMC 1: i) the *translucent* phase that is characterized by molecular hydrogen densities of $1-5\times10^{-3}$ cm^{-3} and is located at visual extinctions of 3−7 mag; ii) the *dense* phase with molecular hydrogen densities of a few 10^4 cm^{-3}, located at A_V > 10 mag. The transition between these two phases (from 7 to 10 mag) occurs in a spatial scale of <0.04 pc and it is not well sampled by our observations. Our data show that carbon, oxygen and sulfur are significantly depleted in the C^+/C/CO transition zone (A_V ~ 3-4 mag) with C/H ~8×10^{-5} , C/O=1, and S/H ~ 8×10^{-7}. The gas phase abundances of C and O decrease by an additional factor of 2 during the translucent phase, i.e. until A_V ~ 10 mag. In contrast, the S/H value remains quite constant in this phase
Conclusions. Based on our results, we propose that the freeze out of CO if the main process that changes the grain composition in the translucent part of the cloud producing a progressive depletion of C and O from A_V~ 3 mag to A_V~ 10. Regarding sulfur, we measure a constant depletion of ~20 across the translucent cloud. In order to account for the chemical composition observed towards the TMC 1-CP core, sulfur depletion should increase by an additional factor of ~10 in the dense cloud .

Key words. Astrochemistry – ISM: abundances – ISM: kinematics and dynamics – ISM: molecules – stars: formation – stars: low-mass

1. Introduction

In recent years, space telescopes such as Spitzer and Herschel have revolutionized our view of star-forming regions. Images of giant molecular clouds and dark cloud complexes have revealed spectacular networks of filamentary structures where stars are born (André et al., 2010). Interstellar filaments are almost everywhere in the Milky Way and are the preferred site for star formation. Now we believe that filaments precede the onset of most star formation, funnelling interstellar gas and dust into increasingly denser concentrations that will contract and fragment leading to gravitationally bound prestellar cores that will eventually form stars.

Gas chemistry has a key role in the star formation process by determining aspects such as the gas cooling and the ionization degree. Molecular filaments can fragment to prestellar cores to a large extent because molecules cool the gas, thus diminishing the thermal support relative to self-gravity. The ionization fraction controls the coupling of magnetic fields with the gas, driving the dissipation of turbulence and angular momentum transfer, and therefore it plays a crucial role in the cloud collapse (isolated vs clustered star formation) and the dynamics of accretion discs (see Zhao et al., 2016; Padovani et al., 2013). In the absence of other ionization agents (X-rays, UV photons, J-type shocks), the ionization fraction is proportional to $\sqrt{\zeta_{H_2}}$, where ζ_{H_2} is the cosmic-ray ionization rate for H_2 molecules, which becomes the key parameter in the molecular cloud evolution (McKee, 1989; Caselli et al., 2002). The gas ionization fraction, X(e^-), as well as the molecular abundances depend on the elemental depletion factors (Caselli et al., 1998). In particular, Carbon (C) is the main donor of electrons in the cloud surface (A_v<4 mag) and, because of its lower ionization potential and as long as it is not heavily depleted, Sulfur (S) is the main donor in the ∼3.7−7 magnitudes range that encompasses a large fraction of the molecular cloud mass. Depletions of C and O determine the cooling gas rate since CO and CII are main coolants in molecular clouds.

Surface chemistry and the interchange of molecules between the solid and gas phases have a leading role in the gas chemical evolution from the diffuse cloud to the prestellar core phase. Elemental depletions constitute a valuable piece of information for our understanding of the grain composition and evolution. For a given element X, the missing atoms in gas phase are presumed to be locked up in solids, i.e., dust grains and/or icy mantles. The knowledge of the elemental depletions would hence provide a valuable information to study the changes in the dust grain composition across the cloud.

GEMS (Gas phase Elemental abundances in Molecular CloudS) is an IRAM 30m Large Program aimed determining the S, C, N, O depletions and X(e^-) as a function of visual extinction, in a selected set of prototypical star forming filaments. Regions with different illumination are included in the sample in order to investigate the influence of UV radiation (photodissociation, ionization, photodesorption) and turbulence (grain sputtering, grain-grain collisions) on these parameters, and eventually in the star formation history of the cloud. This is the first of the series of GEMS papers and it is dedicated to the prototypical dark cloud TMC 1.

2. TMC 1

The Taurus molecular cloud (TMC), at a distance of 140 pc (Elias, 1978; Onishi et al., 2002), is one of the closest molecular cloud complexes and is considered an archetype of low-mass star forming regions. It has been the target of several cloud evolution and star formation studies (Ungerechts & Thaddeus, 1987; Mizuno et al., 1995; Goldsmith et al., 2008), being extensively mapped in CO (Cernicharo & Guelin, 1987; Onishi et al., 1996; Narayanan et al., 2008) and visual extinction (Cambrésy, 1999; Padoan et al., 2002). The most massive molecular cloud in Taurus is the Heiles cloud 2 (HCL 2) (Onishi et al., 1996). TMC 1 was included in the Herschel Gould Belt Survey (André et al., 2010). One first analysis of these data were carried out by Malinen et al. (2012) who generated visual extinction maps of the two long filaments in HCL 2 based on near-IR (NIR) extinction and Herschel data. As one of the most extensively studied molecular filament, TMC 1 is also included in the Green-Bank Ammonia Survey (PIs: R. Friesen & J. Pineda) (Friesen et al., 2017).

TMC 1 has been also the target of numerous chemical studies. In particular, the positions TMC 1-CP and TMC 1-NH3 (the cyanopolyne and ammonia emission peaks) are generally adopted as patterns to compare with chemical codes (Fehér et al., 2016; Gratier et al., 2016; Agúndez & Wakelam, 2013). Less studied from the chemical point of view, TMC 1-C has been identified as an accreting starless core (Schnee et al., 2007, 2010).

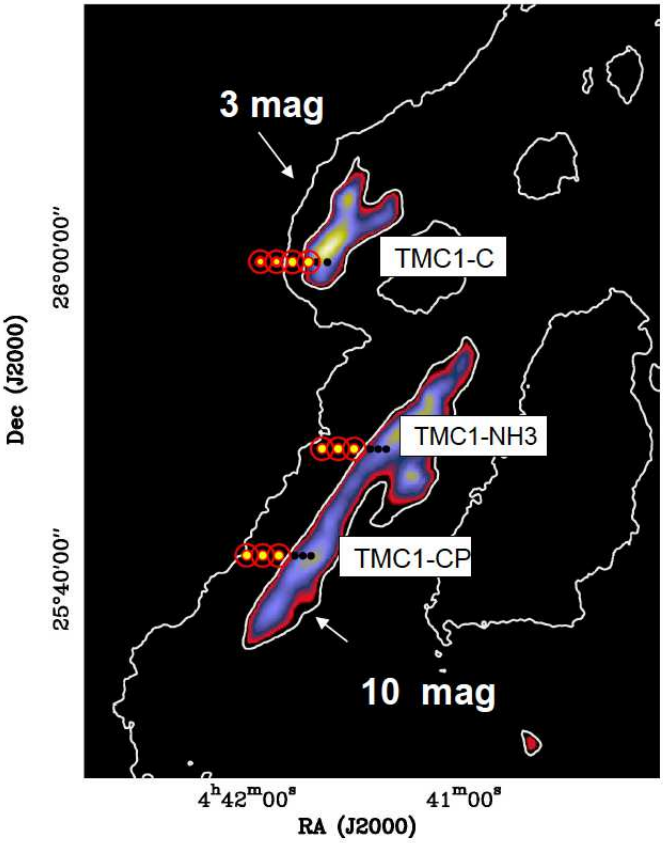

Fig. 1. Visual extinction map of TMC 1 (J. Kirk, 2019, in prep). In order to show up the spatial distribution of dense core component, we have masked in black the regions with A_v<10 mag. The positions indicated with black circles are those only observed with the 30m telescope. The positions marked with red/yellow are those observed with the Yebes telescope, as well. The empty red circle indicated the beam of the 40m telescope in band K (beam∼84"), the red filled circe is the Yebes beam in band Q (beam∼42"), and the yellow circles indicates the beam of the IRAM telescope at 3mm (beam∼29").

Table 1.- Molecular tracers

	$A_V < 10mag$	A_v >10mag
X(e^-)	^{13}CO, HCO^+	^{13}CO, $C^{18}O$, $H^{13}CO^+$, $H^{18}CO^+$
n(H_2)	CS	CS, $C^{34}S$, ^{13}CS, SO, ^{34}SO
C/H	^{13}CO, HCN, CS	^{13}CO, $C^{18}O$, $H^{13}CN$, $HC^{15}N$
O/H	^{13}CO, SO	^{13}CO, $C^{18}O$, ^{34}SO
N/H	HCN	$H^{13}CN$, $HC^{15}N$, N_2H^+
S/H	CS, SO, HCS^+	$C^{34}S$, ^{34}SO, ^{13}CS

3. Observational Strategy

In order to derive the elemental gas abundance of C, O, N and S, we need to determine the abundances of the main gas reservoirs (see Table 1). Essentially, most of the carbon in molecular clouds is locked in CO and the C depletion is derived from the study of CO and its isotopologues. Several works have studied the depletion of CO in dense starless cores and young protostars (Caselli et al., 1999; Kramer et al., 1999; Bacmann et al., 2002; Alonso-Albi et al., 2010; Hernandez et al., 2011; Maret et al., 2013; Miettinen & Offner, 2013; Lippok et al., 2013). The main reservoirs of nitrogen are atomic nitrogen (N) and molecular nitrogen (N_2) which are not observable. The nitrogen abundance needs to be derived by applying a chemical model to fit the observed abundances of nitriles (HCN, HNC, CN) and N_2H^+. The HCN abundance is also dependent on the amount of atomic C in gas phase and hence, on the C/O ratio (Loison et al., 2014). The most abundant oxygenated species, O, H_2O and OH, cannot be observed in the millimeter domain and the oxygen depletion factor has to be derived indirectly. In the case of sulfur, depending on the local physical conditions and the chemical age, atomic S and/or SO are expected to be the main gas phase reservoir in dense clouds (Fuente et al., 2016; Vidal et al., 2017). Unfortunately, the direct observation of atomic S is difficult and, thus far, has only been detected in some bipolar outflows using the infrared space telescope Spitzer (Anderson et al., 2013). Sulfur depletion in molecular clouds is determined from the observation of a few molecular compounds, mainly CS and SO, whose abundances are very sensitive to the C/O gas-phase ratio and time evolution.

Table A.1 and Table A.2 show the the detailed receiver setups and the list of lines observed in each setup. When possible we observe several lines of the same species in order to accurately determing the molecular abundance. When only one line can be observed, we use the molecular hydrogen density derived from the fitting of the CS (and their rarer isotopologues $C^{34}S$ and ^{13}CS) 3→2 and 2→1 lines. Using the wide bandwidth of the 30m receivers, we can observe the most intense 3mm and 2mm lines with only 4 receiver setups (see Table A.2). Towards the edge of the cloud, the densities are lower and the CS 3→2 line is not detected. For this reason we complement the 30m observational dataset with observations of the CS 1→0 line using the 40m band-Q receiver towards those positions with $A_V < 10$ mag (see Fig 1). The 40m configuration allows us to observe simultaneously the NH_3 (1,1) and (2,2) lines in band K. We use these observations to constrain the gas kinetic temperature at the cloud edges.

The high sensitivity required by our project, prohibit the mapping of a large area. Instead, we observe cuts roughly perpendicular to the filaments covering a typical range of A_V from ∼ 3 mag to > 20 mag. In TMC 1, we have observed the three cuts indicated in Fig 1. These are right-ascension cuts (declination is fixed) and cut the dense filament through three well known positions: TMC 1-CP, TMC 1-NH3 and TMC 1-C. The coordinates of these positions are shown in Table 2. These positions are spatially coincident with high extinctions regions, A_V∼ 20 mag. Recent work by Kirk et al. (2019) suggest that TMC 1-C and TMC 1-CP are real cores but TMC 1-NH3 is just a pile-up of dense molecular gas. We have observed 6 positions per cut which corresponds to the offsets (0",0"), (+60",0"), (+120",0"), (+180",0") and (+240",0") relative to the positions listed in Table 2 (circles in Fig 1). The positions marked with black circles have been only observed with the 30m telescope. In addition to the 30m observations, we have observed in band Q and K using the 40m Yebes telescope the positions marked with yellow and red circles.

Table 2. Source coordinates

	RA(J2000)	Dec (J2000)	V_{lsr} (km s^{-1})
TMC 1-CP	04:41:41.90	25:41:27.1	5.8
TMC 1-NH3	04:41:21.30	25:48:07.0	5.8
TMC 1-C	04:41:38.80	25:59:42.0	5.2

4. Data acquisition

4.1. IRAM 30m telescope

The 3mm and 2mm observations were carried out using the IRAM 30-m telescope at Pico Veleta (Spain) during three observing periods in July 2017, August 2017 and February 2018. The telescope parameters at 3mm and 2mm were listed in Table A.1. The observing mode was frequency switching with a frequency throw of 6 MHz well adapted to remove standing waves between the secondary and the receivers. The Eight MIxer Receivers (EMIR) and the Fast Fourier Transform Spectrometers (FTS) with a spectral resolution of 49 kHz were used for these observations. During the 30m observations we used the Frequency-Switching procedure in order to optimize the detection sensitivity. The intensity scale is T_A^* and calibration errors are ∼20%. Although numerous lines are detected in the range of frequencies covered by our observations, specially towards the extinction peaks, in this paper we concentrate in the most abundant molecules (and their isotopologues): CO, HCO^+, HCN, CS, SO, HCS^+, and NNH^+. The rest of species will be analysed in forthcoming papers.

4.2. Yebes 40m telescope

The RT40m is equipped with HEMT receivers for the 2.2-50 GHz range, and a SIS receiver for the 85-116 GHz range. Single-dish observations in K-band (21-25 GHz) and Q-band (41-50 GHz) can be performed simultaneously. This configuration was used to observed the positions marked with a yellow-red circle in Fig 1. The backends consisted of FFTS covering the band of ∼2 GHz in band K and ∼9 GHz in band Q, with a spectral resolution of ∼38 kHz. Central frequencies were 23000 MHz and 44750 MHz for the K and Q band receivers, respectively. The observing procedure was position-switching, and the OFF-positions are RA(J2000):04:42:24.24 Dec(2000):25:41:27.6 for TMC 1-CP, RA(J2000):04:42:29.52 Dec(2000):25:48:07.2 for TMC 1-NH3, RA(J2000):04:42:32.16 Dec(J2000):25:59:42.0 for TMC 1-C. These positions were checked to be empty of emission before the observations. The intensity scale is T_{MB} with conversion factors of 4.1 Jy/K in band Q and in 4.8 Jy/K in band K.

4.3. Herschel Space Observatory: A_V and T_d maps

In this work, we use the column density and dust temperature maps of TMC 1 reported by Kirk et al. (2019, in prep) and created following the process described in Kirk et al. (2013) and Kirk et al. (2019). To help to the understanding of this paper, in the following we give a brief explanation of the methodology. The PACS and SPIRE (Poglitsch et al., 2010; Griffin et al., 2010) data were taken as part of the Herschel Gould Belt Survey (André et al., 2010) and were reduced as described in Kirk et al. (2019, in prep). The absolute calibration (median flux level) of the maps was estimated using data from Planck and IRAS (c.f. Bernard et al., 2010). The data was then convolved to the resolution of the longest wavelength 500 μm (36 arcsec).

A greybody function of the form $F_\nu = MB_\nu(T)\kappa_\nu/D^2$ was fitted to each point where M is the dust mass, $B_\nu(T)$ is the Planck function at temperature T, and D = 140 pc was the assumed distance to Taurus. The dust mass opacity was assumed to follow a standard form with $\beta = 2$ and a reference value of 0.01 cm^2 g^{-1} at 1 Thz. While using the same dust assumptions, the resulting dust map agreed well with the Planck 353 Optical Depth map above $N(H_2) \sim 1.5 \times 10^{21}$ cm^{-2} (Kirk et al. 2019). The typical uncertainty on the fitted dust temperature was 0.3-0.4 K. The uncertainty on the column density was typically 10% and reflects the assumed calibration error of the Herschel maps (Kirk et al. 2019, in prep).

5. Spectroscopic data: Line profiles

Fig A.1 to A.6 show a subset of our spectra across the cuts TMC 1-CP, TMC 1-NH3 and TMC 1-C. The lines of the most abundant species are optically thick at $A_v > 7$ mag and present self-absorbed profiles. However, only the lines of the main isotopologue are detected towards positions with $A_v < 7$ mag. Linewidths vary between ~0.3 to ~1.5 depending on the transition. The largest line widths are measured in the ^{13}CO 1→0 lines with Δv~1.5±0.5. The higher excitation lines of species like CS and SO, and those of the high density tracers HCS$^+$, N_2H^+ and HCN, show Δv ~0.4±0.1. Narrow linewidths are also observed in NH_3 (1,1) and (2,2) inversion lines. These variations in the line widths can be understood as the consequence of the existence of layers with different excitation conditions along the line of sight.

Several authors have discussed the complex velocity structure of the TMC 1 cloud (Lique et al., 2006a; Fehér et al., 2016; Dobashi et al., 2018). Based on high-velocity resolution (0.0004 km s^{-1}) observations of the HC_3N J=5→4 line, Dobashi et al. (2018) propose that the dense TMC 1 filament is composed of at least 4 velocity components at 5.727, 5.901, 6.064 and 6.160 km s^{-1} with small linewidths, ~0.1 km s^{-1}, and a more diffuse component at 6.215 km s^{-1} with a linewidth of ~0.5 km s^{-1}. The velocity resolution of our observations (from 0.27 km s^{-1} at 7mm, to 0.16 km s^{-1} at 3mm and 0.09 km s^{-1} at 3mm) is not enough to resolve these narrow velocity components. In spite of this, in order to have a deeper insight in the velocity structure of the region, we have fitted the observed profiles using 5 velocity components centered at the velocities 5.0, 5.5, 6.0, 6.5, 7.0 km s^{-1} and with a fixed Δv=0.5 km^{-1}. Fig 2 show the result of our fitting for three positions, offsets (+240",0), (+120",0) and (0,0) in the cut across TMC 1-CP. Interestingly, the number of velocity components detected in each line remains constant with the position, even when the position (+240",0) is located 0.16 pc away from TMC 1-CP. However, the number of detected velocity components does vary from one transition to another. The

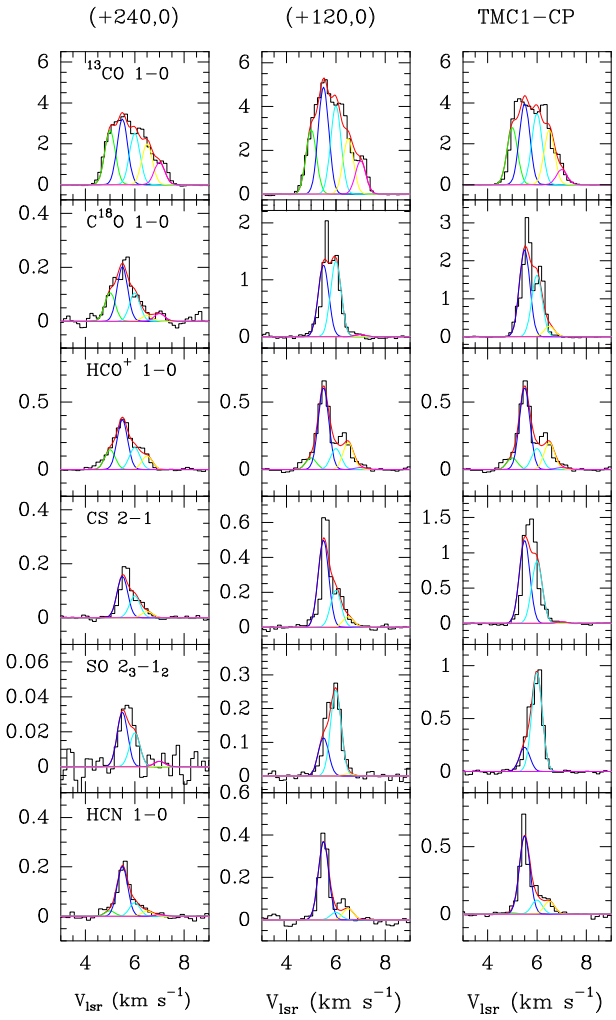

Fig. 2. Selection of 30m spectra towards the offsets (+240",0), (120",0) and (0,0) in the TMC 1-CP cut. In order to investigate the velocity structure we have fitted the observed lines profiles with 5 Gaussians with a fixed linewidth of 0.5 km s^{-1} centered at the velocities 5.0 (green), 5.5 (dark blue), 6.0 (light blue), 6.5 (yellow), 7.0 km s^{-1} (fucsia).

five velocity components appears in the spectra of ^{13}CO 1→0, C^{18}O 1→0, and HCO$^+$ 1→0. The CS 2→1 and SO 2_3→1_2 spectra present intense emission in the 5.5 km s^{-1} and 6.0 km s^{-1} components, and only weak wings atthe other components. Interestingly, only the 5.5 km s^{-1} present intense emission in the HCN spectra. As a first approximation to the comprehension of the gas chemistry, in this paper we use the integrated line intensities to derive column densities and abundances. This is motivated by the limited spectral resolution (at 3mm) and sensitivity (at 2mm) of our observations that introduces large uncertainties in the multi-velocity analysis.

6. Physical conditions: Gas kinetic temperature and molecular hydrogen density

A detailed knowledge of the physical conditions is required for an accurate estimate of the molecular column densities and abundances. This is specially important in those positions where we have observed only one line and a multi-transitional study is not possible. In these cases, the knowledge of the gas kinetic temperature and density is imperative. CS is a diatomic molecule with

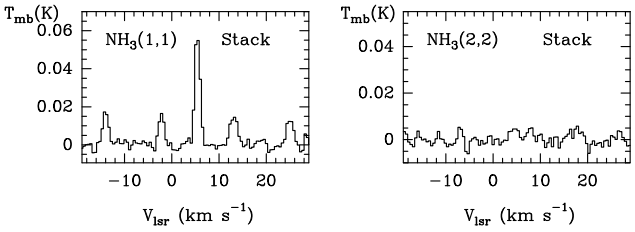

Fig. 3. NH_3 (1,1) and NH_3 (2,2) lines profiles obtained by stacking all the band-K spectra observed with the 40m Yebes telescope (A_V < 10 mag) towards TMC 1.

well known collisional coefficients (Lique et al., 2006b) that has been largely used as density and column density tracer in the interstellar medium. Moreover, the velocity-component analysis presented in Sect. 5 shows that CS is detected in the 5.5 km s^{-1} and 6.0 km s^{-1} components, which encompass the bulk of the dense molecular gas (compare, e.g., the C^{18}O and CS profiles in Fig 2). Therefore, we consider that CS and its isotopologues are good tracers of the average physical conditions in this cloud.

In order to derived the gas physical conditions, we fit the line intensities of the observed CS, C^{34}S and ^{13}CS lines using the molecular excitation and radiative transfer code RADEX (van der Tak et al., 2007). During the fitting process, we fix the isotopic ratios to ^{12}C/^{13}C=60, ^{32}S/^{34}S= 22.5 (Gratier et al., 2016) and let T_k, n(H$_2$) and N(CS) vary as free parameters. The parameter space (T_k, n(H$_2$) and N(CS)) is then explored following the Monte Carlo Markov Chain (MCMC) methodology with a Bayesian inference approach. In particular, we used the emcee (Foreman-Mackey et al. 2012) implementation of the Invariant MCMC Ensemble sampler methods by Goodman & Weare (2010). While n(H$_2$) and N(CS) are allowed to vary freely, we need to use a prior to limit the gas kinetic temperatures to reasonable values in this cold region and hence break the temperature-density degeneracy that is usual in this kind of calculations.

The prior in the gas kinetic temperature is based on our knowledge of the dust temperature from Herschel maps (Kirk et al. 2019). Gas and dust are expected to be thermalized in regions with n(H$_2$)>10^4 cm^{-3}. Friesen et al. (2017) estimated the gas kinetic temperature in wide sample of molecular clouds based on the NH_3 (1,1) and (2,2) inversion lines, and obtained that the gas temperature is systematically ∼1-2 K lower than the dust temperature obtained from the Herschel maps This discrepancy is interpreted as the consequence of the single-temperature SED fitting procedure which assumes that all the dust is at the same temperature along the line of sight. Towards a starless core in which the dust in the surface is warmer than in the innermost region, this approximation would produce an overestimation of the dust temperature. In order to account for these effects, in our mcmc calculations we use a flat prior to the gas kinetic temperature with constant probability for T_k=T_d±5 K and cero probability outside.

In Table 3, we show the gas temperature and the density derived from the multi-line fitting of CS and its isotopologues. Across the cuts, there are two differentiated regions: i) for Av<7.5 mag, the density is quite uniform and equal to ∼ a few 10^3 cm^{-3} and gas temperatures are about 13-15 K which corresponds to gas pressure of ∼5 × 10^4 K cm^{-3}. Hereafter, we will refer to this moderate density envelope as the *translucent* component; and ii) for Av>7.5 mag, the density is an order of magnitude larger, T_k∼10 K and the density keeps increasing until the extinction peak. Hereafter, we will refer to this region as the *dense* component. The gas pressure in the dense phase is about 10 times larger than in the translucent phase. The transition from one phase to the other occurs in < 60" (∼0.04 pc) and it is not well sampled by our data (see Fig 4). In Table 3 we also compare our estimates with previous ones by Fehér et al. (2016) towards TMC 1-CP and TMC 1-NH3, finding excellent agreement. The derived densities for both, the translucent and the dense components, are also in good agreement with previous estimates towards TMC 1-C by (Schnee et al., 2010) and towards TMC 1-CP by (Lique et al., 2006a).

The low densities found in the translucent phase, n(H$_2$)∼ a few10^3 cm^{-3}, might cast some doubts about our assumption of gas and dust thermal equilibrium. In order to check this hypothesis, we have tried to independently derive the gas kinetic temperature in this region using our NH_3 data. For that, we have stacked all the NH_3 (1,1) and (2,2) spectra obtained with the 40m Yebes telescope towards the positions with A_v < 10 mag of the three cuts. The stacked spectra are shown in Fig 3, with a good detection of the NH_3 (1,1) line while the NH_3 (2,2) line remains undetected. Even assuming a density as low as n(H$_2$)=10^3 cm^{-3}, a RADEX calculation shows that the non-detections of the (2,2) line implies an upper limit of < 13 K for the gas temperature, slightly lower than the dust temperature. It is remarkable that NH_3 is only detected in the 5.5 km s^{-1} velocity component while CS is detected in the 5.5 km s^{-1} and 6.0 km s^{-1} components. The upper limit to the gas kinetic temperature is only valid for the 5.5 km s^{-1} component that is very likely the densest and coldest component. We consider, therefore, that the temperature derived from the CS fitting is more adequate for our purposes and it is used hereafter in the molecular abundance calculations. In Sect. 8, we compare the the temperatures obtained with our CS fitting with those predicted with the Meudon PDR code in order to validate this hypothesis.

7. Molecular abundances

Molecular column densities and abundances have been derived using RADEX and the gas temperatures and hydrogen densities shown in Table 3. In the following, we comment details on the abundance calculations.

7.1. ^{13}CO, C^{18}O

In this work, we use ^{13}CO and C^{18}O as tracers of CO by assuming fixed isotopic ratios. We have only observed one ^{13}CO and C^{18}O rotational line and we need to assume the physical condition in Table 3 to derive their column densities. Since the ^{13}CO and C^{18}O J=1→0 lines are thermalized in the range of densities considered, we do not expect any uncertainty because of the adopted densities. The major uncertainty comes from the opacity effects that we try to avoid by observing the two rarer isotopologues.

For A_V> 7 mag, the ^{13}CO 1→0 line is expected to be optically thick (τ > 1). In this region, we use C^{18}O as tracer of the CO abundance by assuming ^{16}O/^{18}O=600. For A_V<7 mag, the ^{13}CO line is expected to be optically thin. In this region we have separately estimated the ^{13}CO and C^{18}O column densities which allows us to investigate the ^{13}CO/C^{18}O abundance ratio. Interestingly, this ratio increases from ∼10 at A_V∼7 mag to ∼40 at A_V∼ 3 mag. This result is not the consequence of the numerous velocity components along the line of sight. As shown in Fig 2, the T_b(^{13}CO 1→0)/T_b(C^{18}O 1→0) is >20 in all the velocity components towards the offset (240",0) relative

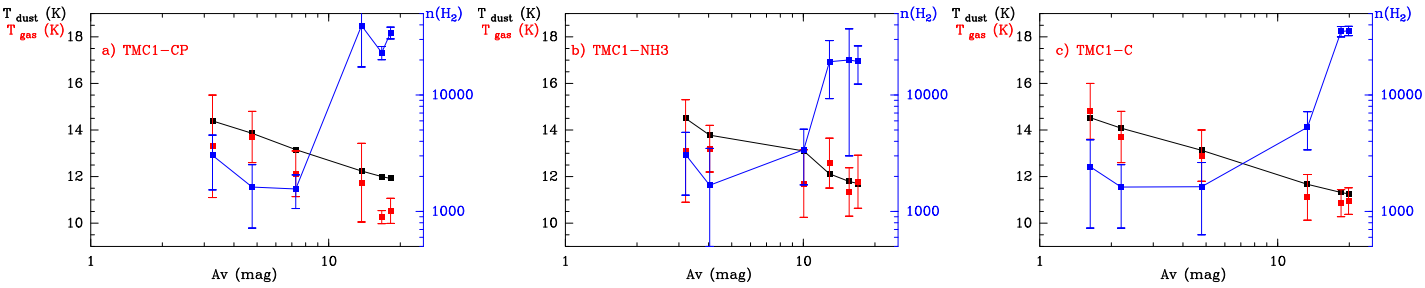

Fig. 4. Lower (black) and upper (red) limits of the molecular hydrogen density adopted in our calculations in the cuts across TMC 1-C, TMC 1-NH3 y TMC 1-CP. In the last panel, we show T_{dust} vs A_V for these three cuts.

Table 3. Physical conditions

Position	HSO (Kirk+18)		GEMS (This work)		NH_3 (Fehér+16)		
	T_d (K)	$N(H_2)$ (cm^{-2})	T_k (K)	$n(H_2)$ ($\times 10^4$ cm^{-3})	T_k (K)	$n(H_2)$ ($\times 10^4$ cm^{-3})	
TMC1-CP+0	11.92	18.20	10.5±0.5	3.4±0.4	10.6±1.1	1.0±0.3	^{13}CS - C^{34}S J=2→1, 3→2
TMC1-CP+30	12.00	16.71	10.3±0.3	2.3±0.3			^{13}CS - C^{34}S J=2→1, 3→2
TMC1-CP+60	12.24	13.74	11.7±1.7	3.9±2.2			^{13}CS - C^{34}S J=2→1, 3→2
TMC1-CP+120	13.16	7.27	12.1±1.0	0.16±0.05			C^{34}S - CS J=1→0, 2→1, 3→2
TMC1-CP+180	13.86	4.77	13.7±1.1	0.16±0.09			C^{34}S - CS J=1→0, 2→1, 3→2
TMC1-CP+240	14.39	3.25	13.3±2.2	0.30±0.15			CS J=1→0, 2→1, 3→2
TMC1-NH3+0	11.70	16.97	11.8±1.1	2.0±0.7	11.0±1.1	1.2±0.3	^{13}CS - C^{34}S J=2→1, 3→2
TMC1-NH3+30	11.79	15.58	11.3±1.0	2.0±1.7			^{13}CS - C^{34}S J=2→1, 3→2
TMC1-NH3+60	12.12	12.88	12.6±1.1	1.9±1.0			^{13}CS - C^{34}S J=2→1, 3→2
TMC1-NH3+120	13.10	10.04	11.7±1.4	0.34±0.17			C^{34}S - CS J=1→0, 2→1, 3→2
TMC1-NH3+180	13.78	4.04	13.2±1.0	0.31±0.18			CS J=1→0, 2→1, 3→2
TMC1-NH3+240	13.10	2.18	13.1±2.2	0.32±0.17			CS J=1→0, 2→1, 3→2
TMC1-C+0	11.26	19.85	10.9±0.6	3.6±3.3			^{13}CS - C^{34}S J=2→1, 3→2
TMC1-C+30	11.32	18.47	10.9±0.6	3.5±3.6			^{13}CS - C^{34}S J=2→1, 3→2
TMC1-C+60	11.67	13.34	11.1±1.0	0.53±0.19			^{13}CS - C^{34}S J=1→0, 2→1, 3→2
TMC1-C+120	13.13	4.79	12.9±1.1	0.16±0.10			C^{34}S - CS J=1→0, 2→1, 3→2
TMC1-C+180	14.08	2.20	13.7±1.1	0.16±0.09			C^{34}S - CS J=1→0, 2→1, 3→2
TMC1-C+240	14.53	1.63	14.8±1.2	0.24±0.17			CS J=1→0, 2→1, 3→2

to TMC 1-CP. Similarly $T_b(^{13}CO\ 1{\rightarrow}0)/T_b(C^{18}O\ 1{\rightarrow}0){\sim}4$ in all velocity components towards the offset (120",0). The high $N(^{13}CO)/N(C^{18}O)$ ratio is more likely the consequence of selective photodissociation in the translucent cloud (Liszt & Lucas, 1996; Bron et al., 2018). We will discuss this phenomenon in Sect. 8 by comparison of our results with the Meudon PDR code predictions. In order to estimate the CO abundance in the translucent phase, we have used the ^{13}CO column density and assumed the $N(^{12}CO)/N(^{13}CO)=60$

In Fig. 5, we plot the CO abundance estimated as described above as a function of $N(H_2)$, dust temperature and density in the three observed cuts. The CO abundance is well correlated with the dust temperature with a peak abundance of $1.3{\times}10^{-4}$ at Av ∼ 3 mag (T_d=14 K) and decreases by a factor of ∼2 towards the dense core phase. This is the expected behavior in this dark cloud, where the dust temperature is lower than the evaporation temperature (T_{evap}=15-25 K) towards all the observed positions. In order to characterize the variation in the abundances of the studied species towards the extinction peaks, we define the parameter MD(X) as the ratio between the maximum abundance in the translucent phase over the abundance towards the extinction peak. This ratio is calculated for each cut individually and is shown in Table 4. We do not detect significant differences among the cuts.

7.2. HCO^+, $H^{13}CO^+$, $HC^{18}O^+$

We have observed the J=1→0 rotational lines of the HCO^+, $H^{13}CO^+$ and $HC^{18}O^+$. Column densities of all isotopologues have been derived using RADEX and the physical parameters in Table 3. In our column density calculations, we only use the $H^{13}CO^+$ and $HC^{18}O^+$ spectra because the HCO^+ J=1→0 lines present self-absorbed profiles. Then, we derive the HCO^+ column density from the rarer isotopologues assuming $N(HCO^+)/N(H^{13}CO^+)$=60 or $N(HCO^+)/N(HC^{18}O^+)$=600. The results are shown in Fig 5. The HCO^+ abundance is maximum at A_V∼5 mag, i.e., 2 mag deeper than CO in in the translucent cloud. For simplicity, hereafter we will refer to the region at A_V∼5 mag as T1. The abundance of HCO^+ further decrease in the dense component but, in contrast to CO, the value of MD varies from one cut to another. In detail, $MD(HCO^+)$ is ∼10 across TMC 1-CP and TMC 1-C and $MD(HCO^+)$∼2 towards TMC 1-NH3 (see Table 4), suggesting a different density structure or chemical age for the latter.

7.3. CS, $C^{34}S$, ^{13}CS

The CS column densities have been derived as explained in Sect. 6. We find that the CS abundance is maximum in T1, with abundances ∼ $4{\times}10^{-8}$. The dispersion in the derived CS abun-

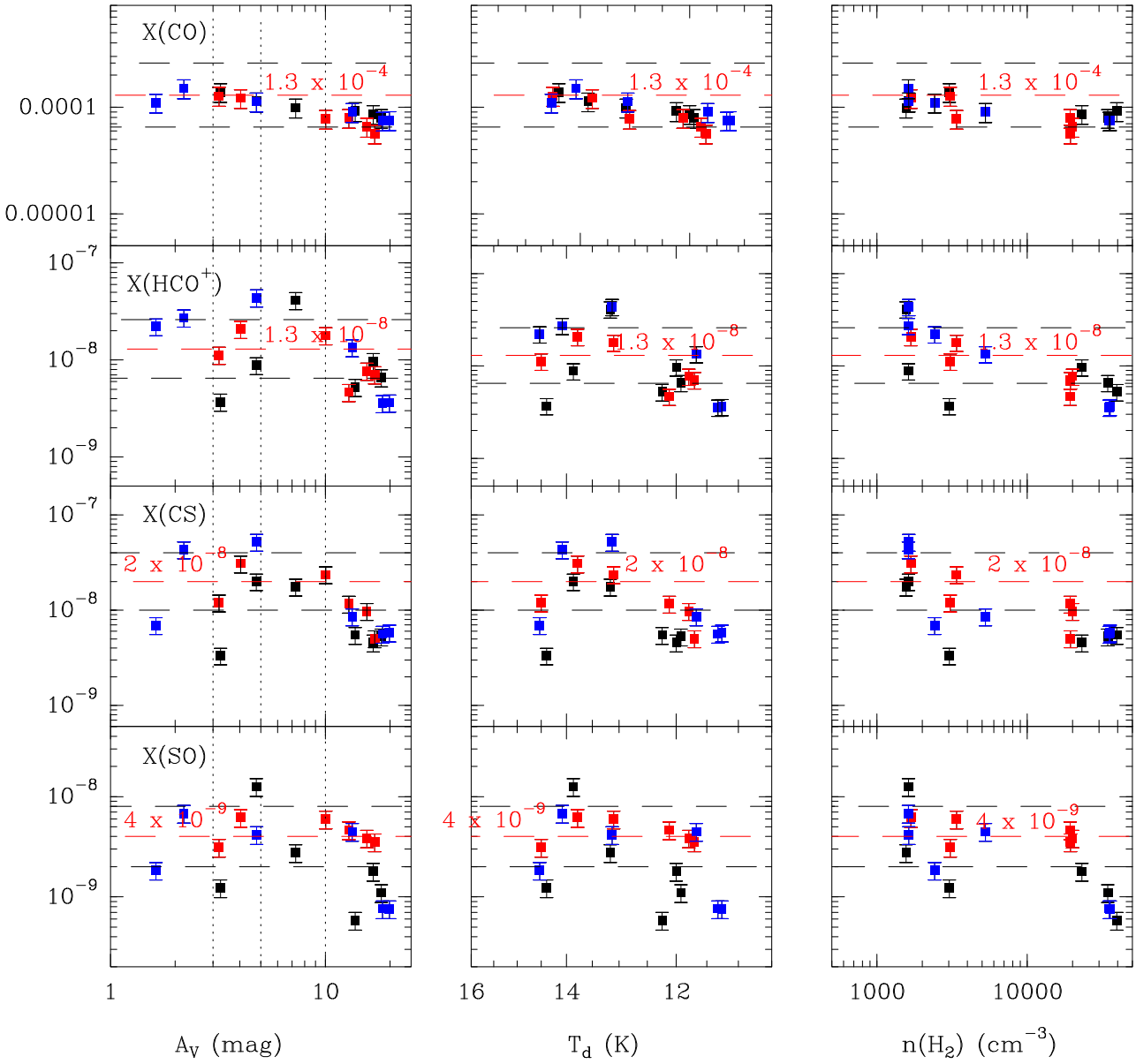

Fig. 5. Estimated molecular abundances wrt H_2 for the three studied cuts, TMC 1-CP (black squares), TMC 1-NH3 (red) and TMC 1-C (blue) as a function of the visual extinction (left column), dust temperature (center panel) and molecular hydrogen densities (right panel).

dances in T1 and T2 is of a factor of 2. For A_v >10 mag, the CS abundance sharply decreases suggesting a rapid chemical destruction or freeze out on the grain mantles. The measured depletion is quite uniform towards the three extinction peaks, MD(CS)= 6±2, with the maximum value towards TMC 1-C.

7.4. SO, ^{34}SO

Several lines of SO and ^{34}SO lie in frequency range covered by our setups (see Table A.2). However, only one ^{34}SO line, J=$2_3 \rightarrow 1_2$, has been detected towards the TMC 1-CP, TMC 1-NH3 and TMC 1-CP cuts. Towards the positions where we detect ^{34}SO line, we measure T_b(SO $2_3 \rightarrow 1_2$)/T_b(^{34}SO $2_3 \rightarrow 1_2$) of 10−20. This implies opacities <2, i.e. the emission of this SO line optically thin or slightly optically in the dense region. Therefore, we estimate the SO column density based on the RADEX fitting of the main isotopologue lines in the dense and translucent phases and we estimate an uncertainty of a factor of 2 in the column density estimates because of the moderate opacity. The derived SO abundances are 0.76 $\times 10^{-9}$, 1.0 $\times 10^{-9}$ and 3.6 $\times 10^{-9}$ for TMC 1-C, TMC 1-CP and TMC 1-NH3, respectively. Our measurement towards TMC 1-CP is consistent with previous estimates by Ohishi & Kaifu (1998), Agúndez & Wakelam (2013) and Gratier et al. (2016).

Similarly to HCO^+ and CS, SO presents its maximum abundance in T1 with a peak value of $\sim 10^{-8}$. The SO depletion towards TMC 1-NH3 is MD(SO)~2 while MD(SO)~10 towards TMC 1-C and TMC 1-CP. The overabundance of SO towards TMC 1-NH3 has been already pointed out by several authors Lique et al. (2006a).

7.5. HCS^+

Although we observed two lines of HCS^+, J=2→1 (all positions) and J=1→0 (positions with A_V<10 mag), we only have one detected line per position since the J=2→1 line is not detected in the translucent part. Moreover we have very few detections in this moderate density region (see Fig 6). Therefore, we are not

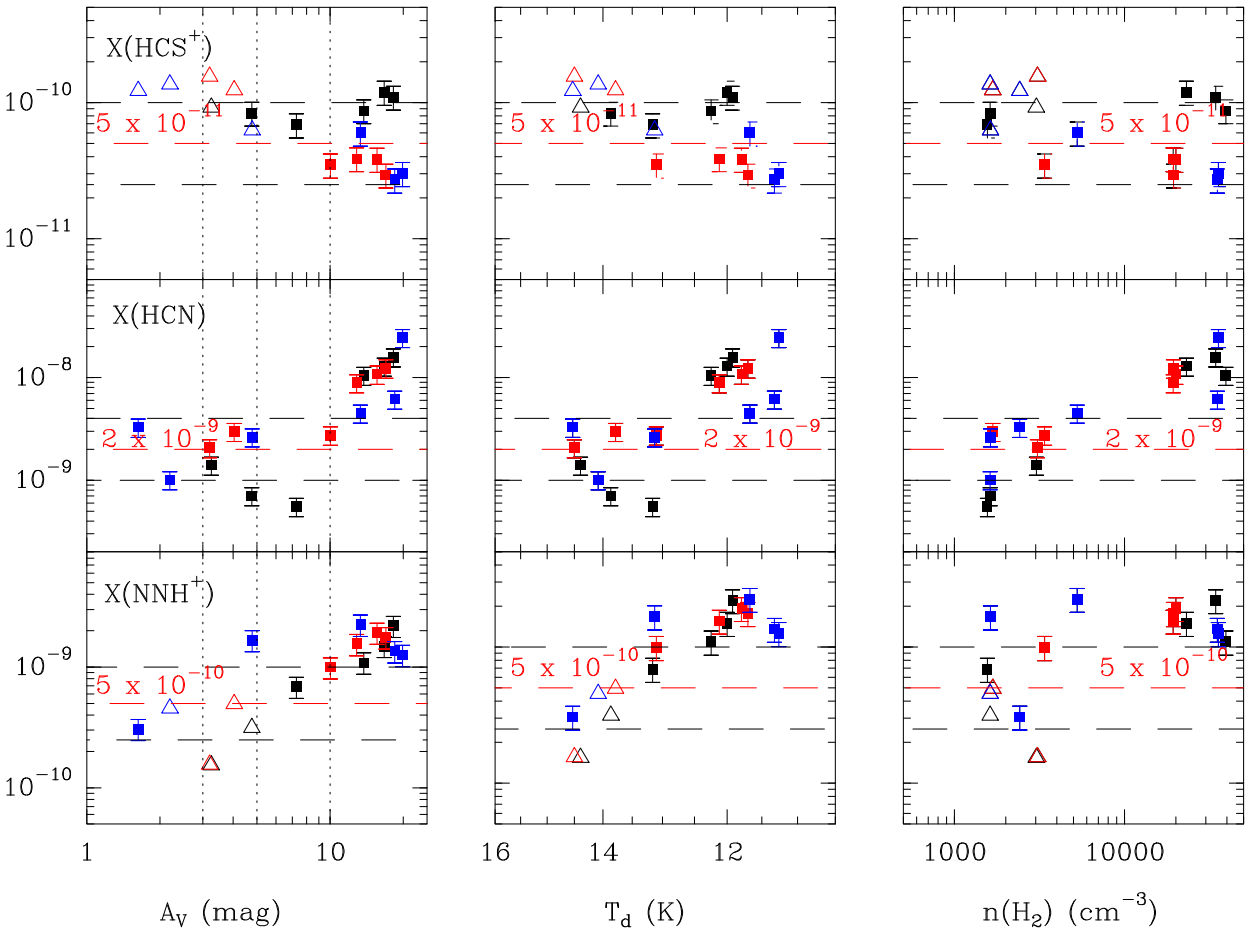

Fig. 6. Estimated molecular abundances wrt H_2 for the three studied cuts, TMC 1-CP (black squares), TMC 1-NH3 (red) and TMC 1-C (blue) as a function of the visual extinction (left column), dust temperature (center panel) and molecular hydrogen densities (right panel). Empty symbols correspond to upper limits.

able to determine any trend of the HCS^+ abundance with the visual extinction. Interestingly, we find differences among the HCS^+ abundance towards the different cuts, being larger towards TMC 1-CP than towards TMC 1-NH3 and TMC 1-C (see Fig 6).

7.6. HCN, $H^{13}CN$, $HC^{15}N$, NNH^+

All the N-bearing species included in this sebsection present larger abundances towards the dense phase than towards the outer part of the cloud. In terms of the parameter $MD(X)$, $MD(X) > 1$ in the three cuts studied in TMC 1. Morever, only the 5.5 km s^{-1} component is detected in the translucent and dense phases.

As commented above, the emission of HCN is mainly coming from the 5.5 km s^{-1} layer and the densities derived from CS might not be adequate. Fortunately, the hyperfine splitting allows us to estimate of the opacity and excitation temperature (assuming a beam filling factor of 1) and hence, an accurate estimate of the density and column density using RADEX. with the collisional coefficients of Dumouchel et al. (2010). In the dense region, we use the isotopologue $H^{13}CN$ in our calculations because the HCN 1→0 line presents deep self-absorption features. Assuming N(HCN)/N($HC^{13}CN$)=60, our calculations give HCN abundances of a few 10^{-8} and molecular hydrogen densities of $5\text{-}10 \times 10^4$ cm^{-3} in the dense cloud. It is remarkable the the densities derived from the HCN data are larger than those derived from CS by a factor of ∼5-10. This is consistent with the interpretation of the 5.5 km s^{-1} velocity component being the densest and coldest one.

Only the HCN 1→0 line is detected in the translucent cloud. Besides, only the the 5.5 km s^{-1} velocity component is detected. From our HCN data and following the procedure described above, we derive densities ∼10^4 cm^{-3} and X(HCN)∼2×10^{-9} (see Fig 6). One interesting point is that the gas with n(H_2)<10^4 cm^{-3} cannot significantly emit in the HCN 1→0 line regardless of the HCN column density. Because of the large dipole moment of HCN, densities >10^4 cm^{-3} are required to achieve excitation temperatures > 5 K and hence detectable emission. This means that our observations cannot probe the HCN abundance in the translucent medium where densities <10^4 cm^{-3} are expected and the abundance we have derived in only a lower limit to the real one. The widespread detection of HCN in diffuse molecular gas (Liszt & Lucas, 2001) with abundances wrt H_2 of ∼4×10^{-9} suggests that our abundance estimate in the translucent cloud must be considered a a lower limit to the real value.

Similarly to HCN, we have fitted the excitation temperature and opacity of the NNH^+ 1→0 line based on the hyperfine splitting, and hence the total NNH^+ column densities. This molecular ion has been detected towards the dense region with abundances of about 1×10^{-9} at 10 mag which increase to ∼ 2×10^{-9} in the visual extinction peak and densities of a few 10^4 cm^{-3}. Towards the translucent cloud, we have very few detections.

Table 4: Molecular abundances and depletions in TMC 1

Mol	TMC 1-CP	TMC 1-NH3	TMC 1-C
CO	7.9×10^{-5}	5.7×10^{-5}	7.5×10^{-5}
HCO^+	6.5×10^{-9}	7.0×10^{-9}	3.6×10^{-5}
HCN	1.6×10^{-8}	1.2×10^{-8}	2.4×10^{-8}
CS	5.3×10^{-9}	5.0×10^{-9}	5.8×10^{-9}
SO	1.0×10^{-9}	3.6×10^{-9}	7.6×10^{-10}
HCS^+	1.0×10^{-10}	3.0×10^{-11}	3.0×10^{-11}
NNH^+	2.2×10^{-9}	1.8×10^{-9}	1.2×10^{-9}
MD(CO)	1.7	2.2	1.9
MD(CS)	3.8	6.2	8.6
MD(HCO^+)	10	2.8	12
MD(SO)	12	1.7	8.9
MD(H_2S)	25	3.3	66
MD(HCS^+)	0.9	1.2	2.0
MD(NNH^+)	0.3	0.5	1.3
MD(HCN)	0.1	0.2	0.1
HCO^+/CO	8.2×10^{-5}	1.2×10^{-4}	4.8×10^{-5}
HCN/CO	2.0×10^{-4}	2.2×10^{-4}	3.2×10^{-4}
CS/SO	5.3	1.0	7.6
HCS^+/CS	1.9×10^{-2}	8×10^{-3}	5.2×10^{-3}

8. Chemical modeling of the translucent cloud

The increase in dust temperature at the edges of molecular clouds is understood as the consequence of dust heating by the surrounding UV field. Moreover, the high N(^{13}CO)/N(C^{18}O) ratio measured in TMC 1 testifies that UV radiation has an active role in the molecular chemistry. However, the value of the ambient UV field is not established and can vary from one region to another and even between different regions in the same cloud since it depends on the star formation activity in the surroundings. To determine the value of the ambient UV field is hence a requisite for the appropriate chemical model of the region.

8.1. Estimate of the incident UV field in TMC 1

Dust temperatures are determined by the radiative equilibrium balance between the absorption of UV photons and the emission at a given temperature, T_d. The exact value of T_d depends on the ambient UV field and the absorption efficiencies of grains that are dependent on the grain composition and size. The direct calculation of the local UV field as a function of the dust temperature is hampered by our poor knowledge of the grain composition and its detailed variation across the cloud. Alternatively, we can try to fit the observational data with a simple analytical expression. Different attempts have been done to derive parametric expressions that relates the UV ambient field and the dust temperature as a function of the visual extinction (Hollenbach et al., 1991; Zucconi et al., 2001; Garrod & Pauly, 2011; Hocuk et al., 2017). Most of them provide a good fitting of the observed T_d as a function of the incident UV field, χ_{UV}, in a given range of visual extinctions but have problems to fit the whole range, from A_V=0.01 to A_V>50 mag. We have used the most recent parametric expression by Hocuk et al. (2017) to obtain an estimate of the incident UV field. This expression is well adapted to the range of visual extinctions relevant in this paper (3 mag < A_V < 20 mag) and is consistent with what one would expect for a mixed carbonaceous-silicate bared grains.

$$T_d = [11 + 5.7 \times \tanh(0.61 - \log10(A_V))]\chi_{UV}^{1/5.9} \quad (1)$$

where X_{UV} is the UV field in Draine units. Fig 7 shows the T_d-A_V plots for the 3 cuts considered in this paper. None of the cuts can be fitted with a single value of the UV field. In fact, the dense cloud (A_V> 7.5 mag) is better fitted with χ_{UV}~10 while the translucent cloud is fitted with χ_{UV}~ 3. Moreover, the three observed cuts share the same behavior without any hint of variation of χ_{UV} from one cut to another (see Fig 7). One compelling possibility is that this break at A_V> 7.5 mag is caused by a change in the grain properties. A thick layer of ice would allow the dust to be warmer by up to 15% at visual extinctions > 10 mag, i.e., the dense component (Hocuk et al., 2017). In fact, if we decrease the dust temperature in the dense regions by this factor, we could explain all the positions with χ_{UV}~3. This interpretation is also consistent with the sharply decrease in the abundances of the C- and S- bearing molecules with visual extinction in the dense phase. We cannot discard, however, to have an asymmetric illumination of the cloud. Ebisawa et al. (2018) proposed the existence of a warm gas component, T_k~40 K, located at the SW of the TMC 1 filament. In our chemical discussion, we will consider the chemical model results between χ_{UV} ~1 and 10 in order to investigate the impact of the possible errors in our estimate of the UV radiation on the chemistry.

8.2. C, O, and S depletion

We use the steady state gas-phase Meudon PDR code to estimate the C, O and S elemental abundances. In our calculations we assume an isobaric plane-parallel 50 mag cloud with a constant pressure of 5×10^4 K cm^{-3}. This model satisfactorily reproduces the density structure of the translucent part of the TMC 1 cloud. Our cloud is illuminated with a UV field of χ_{UV} =10 from the right side and χ_{UV} =1 from the left side in order to investigate the effect of a modest change in the incident radiation field. The Meudon PDR code does not consider any process of adsorption and desorption of molecules from grains. In order to fit the elemental depletions we just force the initial elementary abundances to values below the solar value.

We have run a series of models in order to explore the parameters space to determine the values of the cosmic ray ionization rate and elemental abundances that best fit our observations (see Table 5). Fig. 8 shows the predicted X(CO), X(HCO^+)/X(CO), X(CS) and X(CS)/X(SO) ratio as a function of the visual extinction for these models. For clarity, we only show the right side (χ_{UV}=10) in this Figure. In Fig. 9 we will compare the predicted abundances in both faces (χ_{UV}=10 and χ_{UV}=1) to show the influence of the adopted χ_{UV} in our results. In the first column of Fig. 8, we show the behavior of the observed abundances under changes in the C/H. For A_V >3 mag, all the carbon atoms are basically locked in CO and C/H is well determined from the measured CO abundance. Our peak CO abundance, ~1.4×10^{-4} show that even at the low extinction of A_V = 3 mag, carbon is depleted by a factor of ~2 and the carbon depletion increases to reach values of ~3−4 at A_V~10 mag. This result is also valid for the case of χ_{UV}=1 (see Fig. 9). In the second column, we investigate the chemical effect of varying $\zeta(H_2)$. The value of $\zeta(H_2)$ mainly affects the predicted X(CS) and the X(HCO^+)/X(CO) abundance ratio. The abundance of CS is strongly dependent on the poorly known value of S/H. Then, we prefer to use X(HCO^+)/X(CO) as a probe of $\zeta(H_2)$ in this first iteration. Based on the X(HCO^+)/X(CO) ratio we estimate that $\zeta(H_2)$ ~5−10 $\times10^{-17}$ reasonable fit the observed ratio in TMC 1. Only the points corresponding to TMC 1-C lies over model prediction. Moreover, this value is consistent with measurements at carried in moderate extinction region (Caselli et al., 1998;

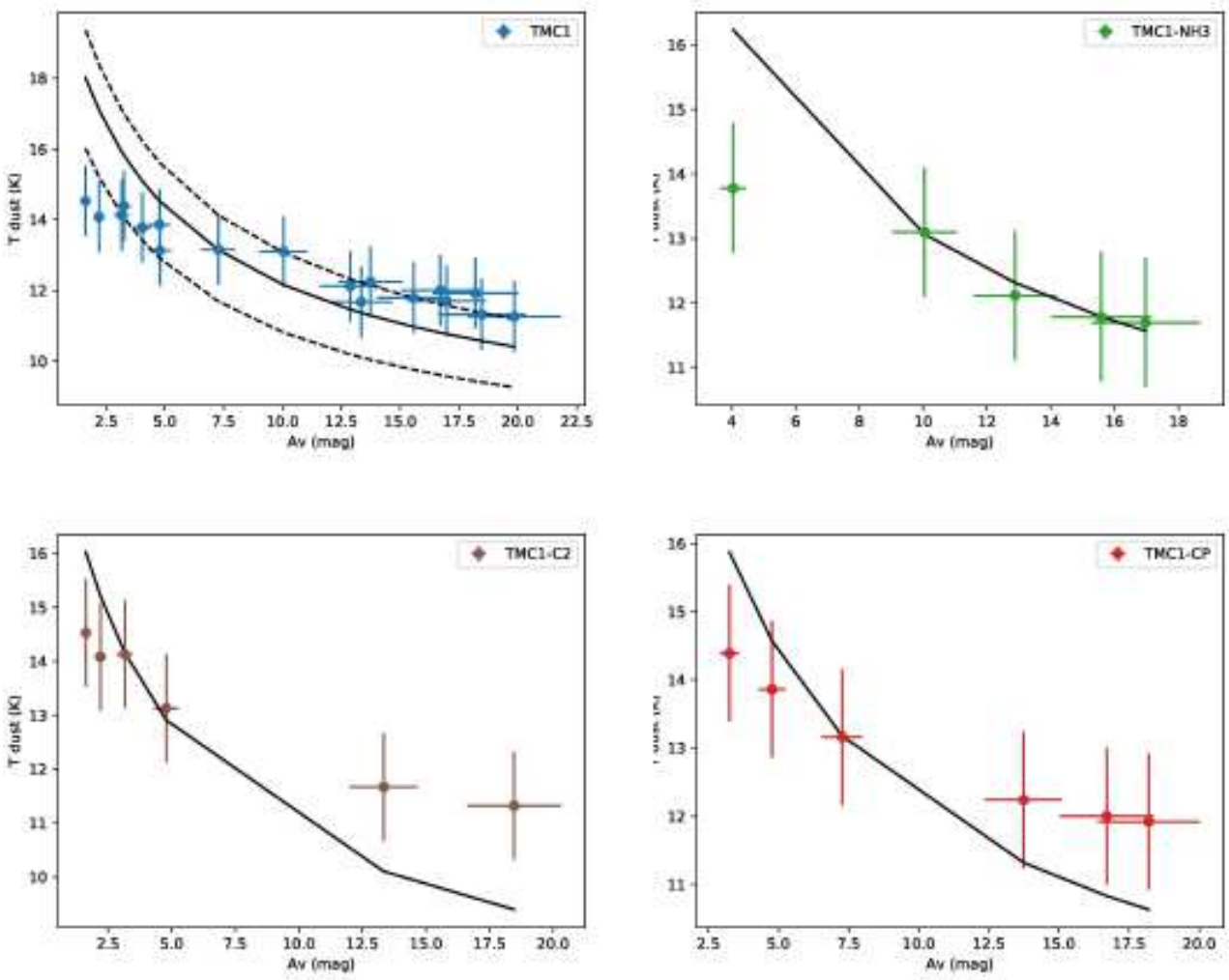

Fig. 7. Dust temperature fit for the three different TMC 1 cuts: TMC 1-CP in (a), TMC 1-NH3 in (b), and TMC 1-C in (c), according to Hocuk et al. (2017) parameterization. We also show the fits in the magnitude ranges discussed before (dashed lines) together with the average fit (solid line) for TMC 1 in (d). For A_V < 7.5, the best fit is found for χ_{UV} ~ 3, as shown in (c). For A_V > 7.5, the best fit corresponds to χ_{UV} ~ 10, as seen in (b). The average value of χ_{UV} ~ 6.5 is found to provide the best fit for the filament TMC 1-CP (a), and the whole TMC 1 region (d).

Padovani et al., 2009). We note but it is significantly Vidal et al. (2017) and Agúndez & Wakelam (2013) estimated a much lower value, ~ 1.3×10^{-17}, towards TMC 1-CP, hence suggesting a variation of $\zeta(H_2)$ into the cloud. The X(HCN)/X(CO) as well as X(CS)/X(SO) abundance ratios are highly dependent on the C/O gas phase elemental ratio (third column of Fig. 8). We have not been able to fit both ratios with a single C/O value. While the observed X(HCN)/X(CO) is well explained with C/O~0.4, X(CS)/X(SO) points to a value of the C/O ~1. As commented in Sect. 4.5, the HCN abundance might be severely underestimated in this moderate density gas. Therefore, we consider that X(CS)/X(SO) is a more reliable tracer of the C/O ratio. Note also that the X(CS)/X(SO) ratio is not very dependent on the S/H value (column 4 of Fig. 8 which support the usage of this ratio to determine C/O. Interestingly, there is not systematic trend of the X(CS)/X(SO) ratio in the translucent cloud that could be identified with a preferential oxygen depletion in this range of visual extinctions. Once the values of $\zeta(H_2)$ and C/O are fixed, the abundances of CS and SO depend almost linearly with S/H (column 4). Our results are best fit with S/H~8×10^{-7}, i.e., a factor of 20 lower than the solar value, S/H ~1.5×10^{-5}. Vidal et al. (2017) estimated S/H~8×10^{-8} towards the TMC 1-CP dense core, i.e, the sulfur depletion increases by an additional factor of 10 during the dense phase.

Following the analysis above described, we propose that C/H~7.9×10^{-5}, C/O~1, and S/H~8×10^{-7}, are the most likely values in the translucent cloud. To further confirm our results, in Fig 9 we compare our "best-fit" model in the two faces of the cloud (χ_{UV}=10 in solid lines and χ_{UV}=1 in dashed lines) with observations. For A_V > 4 mag, the predictions are essentially the same for χ_{UV}=10 and χ_{UV}=1 proving that our results are therefore robust. Most of the abundances and abundance ratios are well fitted with our "Best-fit" model. Only the N(^{13}CO)/N(C^{18}O)) ratio and the HCN abundance are poorly reproduces by our model. The value of the estimated value of the N(^{13}CO)/N(C^{18}O)) ratio for A_V <7.5 mag is larger by a factor <2 than model predictions for the two values of χ_{UV} considered. We do not have an easy explanation for this discrepancy although geometrical effect or the existence of a diffuse envelope could help to improve the agreement. In addition, our fit fails by almost one

Table 5 .- Chemical models

	ζ (s^{-1})	C/H	C/O	S/H
A	5×10^{-17}	1.38×10^{-4}	0.4	1.5×10^{-5}
B	5×10^{-17}	7.90×10^{-5}	0.4	1.5×10^{-5}
C	5×10^{-17}	3.90×10^{-5}	0.4	1.5×10^{-5}
D	5×10^{-18}	1.38×10^{-4}	0.4	1.5×10^{-5}
E	1×10^{-16}	1.38×10^{-4}	0.4	1.5×10^{-5}
F	5×10^{-17}	1.38×10^{-5}	1.0	1.5×10^{-5}
G	5×10^{-17}	7.90×10^{-5}	1.0	8.0×10^{-7}
Best-fit	5×10^{-17}	7.90×10^{-5}	1.0	8.0×10^{-7}

order of magnitude to account for the observed HCN abundance. As commented above, our estimate of the HCN abundance is quite uncertain and need to be understood as a lower limit to the real one. This large uncertainty in the abundances of HCN and N_2H^+ also prevent us from give a reliable estimate of the N/H abundance in the translucent phase.

9. Dense phase

The Meudon PDR code is not adequate to interpret the dense core region where the selective freeze-out of molecules have a dominant role in the chemistry and time-dependent effects are expected to be important (see e.g. (Vidal et al., 2017)). In this paper, we would do only a phenomenological analysis of the chemical changes observed across the dark core region. The abundance of most molecules decreases with the visual extinction from A_V = 10 to 20 mag. The only exceptions are HCN and NNH^+ whose abundance increases towards the dense phase in the three cuts without any significant difference between the cold cores TMC 1-C and TMC 1-CP, and the high extinction peak TMC 1-NH3. We cannot conclude about HCS^+ since this ion has only been detected in the dense phase and our upper limits to the HCS^+ abundance in the translucent phase are not significative. MD(CO), MD(HCO^+), MD(CS) and MD(SO) >1 in the three studied cuts. However, there are significant differences between them. In the case of CO and CS, their abundances decrease only by a factor of 2 from the translucent phase to the dense core. Besides, we do not detect any difference between the high extinction peaks and the cold cores. In contrast, the MD(HCO^+) and MD(SO) decreases by more than one order of magnitude towards TMC 1-CP and TMC 1-C. The large value of MD(HCO^+) might be associated with the change in the cosmic ray ionization rate and consequently in the gas ionization degree in dense regions. The high value of MD(SO) is very likely more related with the freeze out of S- and O-bearing molecules onto the grain mantles.

10. Gas chemical composition from the diffuse to the translucent phase

In general we refer to the gas with densities of $n_H < 100$ cm^{-3} and T_k~100 K as diffuse gas. In this phase, the gas is partially in atomic form and CO is not a good tracer of the molecular gas content. The molecular content of the diffuse gas has been determined by a series of studies based on the molecular absorption lines at mm wavelengths which revealed a surprisingly rich chemistry (see Liszt et al., 2018 and references therein). Translucent clouds are characterized by n_H ~ a few 1000 cm^{-3}, T_k~20−30 K and the gas is mostly in molecular form, CO being a good mass tracer. The higher densities of this phase allows to carry out a chemical study based on molecular emission lines but only the low excitation lines of each species are detected. Although difficult, the comparison of the chemical composition of the diffuse and translucent phases might provide important clues for the understanding of the chemical evolution of the gas in the interstellar medium. All the species studied in this paper except N_2H^+ and HCS^+ have been detected in the diffuse gas. Interestingly, N_2H^+ and HCS^+ have been detected in our survey towards T1. Liszt & Lucas (2001) measured $N(N_2H^+)/N(HCO^+)$ < 0.002 towards 3C111. This quasar is actually seen through a small hole (region of lower than average extinction) in an outlying cloud in the Taurus cloud complex (Lucas & Liszt, 1998). In Fig 10 we show the comparison of the abundances wrt H_2 of the studied molecules with those from our survey. The data towards 3C111 are indicated. There is a large dispersion in the plot of the molecular abundances as a function of the visual extinction. We recall that diffuse clouds are not only characterized by low values of the visual extinction but also for low hydrogen densities. Besides, the visual extinction measured along the line of sight is not necessarily related to the local UV field in diffuse gas with several clouds along the line of sight. One can find a better correlation if one considers the abundances vs the local density and assume that in the diffuse gas the local density is around 50-100 cm^{-3}. For HCO^+, SO and CS we find a trend with their abundances increasing with density from the diffuse to the translucent phase. All these molecules present their peak abundances in T1. HCN might be the only exception to this rule with lower abundances in the translucent phase than in the diffuse gas. As discussed above, the HCN column densities might be severely underestimated in the translucent cloud.

11. Elemental depletions and grain growth

The depletion of an element X in the ISM is defined in terms of its reduction factor below the expected abundance relative to that of hydrogen if all of the atoms were in the gas phase,

$$[Xgas/H] = logN(X)/N(H) - log(X/H)_\odot \quad (2)$$

In this expression, N(X) is the column density of element X and N(H) represents the column density of hydrogen in both atomic and molecular form, i.e., N(H I) + 2N(H_2). The missing atoms of element X are presumed to be locked up in solids within dust grains or in the icy mantle. In the diffuse gas, atomic absorption lines can be used to determine abundances by comparison with the atomic and molecular hydrogen column densities measured through Lyman alpha and Lyman-Werner transitions.Jenkins (2009) present a comprehensive study of the elemental depletions in diffuse clouds. In general, depletions increase with the average density along the line of sight. However, depletions are observed to vary from one line of sight to another. (Savage & Sembach, 1996) interpreted these variations in terms of averages of warm (presumably low density) gas and cool (denser) gas. In his review, Jenkins (2009) distinguish between two cases, "minimum" and "maximum" depletion in the diffuse as which characterize the range of these variations.

In this work, we derive the elemental abundances in the translucent part of TMC 1 on the basis of molecular observations and chemical modelling in the translucent phase. In Table 6 we compare our estimates with previous measurements in diffuse clouds. Our values are not far from the "maximum depletion" case of Jenkins (2009) for C and O. In the translucent phase, we observe a smooth increase in the C and O depletion, while the C/O ratio is quite constant. The freeze out of CO could

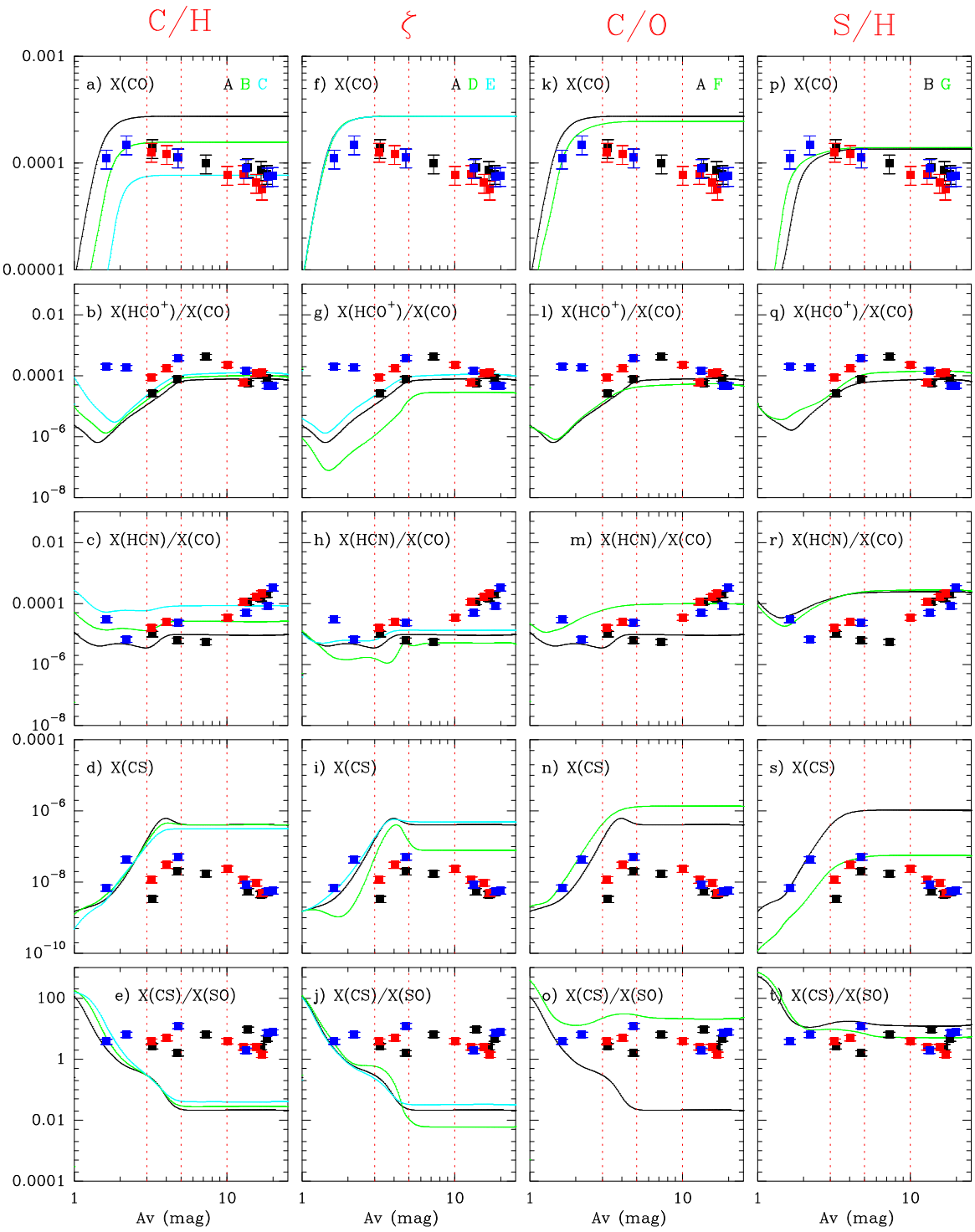

Fig. 8. Comparison between the predictions of models listed in Table 5 and the molecular abundances derived in TMC 1. In this figure, we have selected X(CO), X(HCO^+)/X(CO), X(HCN)/X(CO), X(CS) and X(CS)/X(SO) to explore the parameter space.The observational points are indicated with squares and different color corresponds to the three observed cuts as follows: black for TMC 1-CP, red for TMC 1-NH3 and blue for TMC 1-C.

be the main process that changes the grain composition in this region. Regarding sulfur, we measure a lower value of depletion of ∼20 in the translucent cloud. Although some authors like Jenkins (2009) casts doubts on this interpretation, it is widely accepted that sulfur is not depleted in diffuse clouds (see also Neufeld et al., 2015). Adopting this scenario, sulfur atoms (or ions) should be massively incorporated to dust grains from the HI/H_2 (A_V∼1.5) to the CII/CI/CO transition phases (A_V∼3 mag) to reach a depletion of ∼20 in the translucent medium. However, during the translucent phase the sulfur depletion does not seem to increase.

In Table 6 we also compare the depletions estimated in the translucent part of TMC 1 with those adopted to explain the chemical composition towards the TMC 1-CP dense core. While carbon and oxygen depletions increase only by a factor of 2, sulfur depletion need to be increased to a value of ∼200 to account

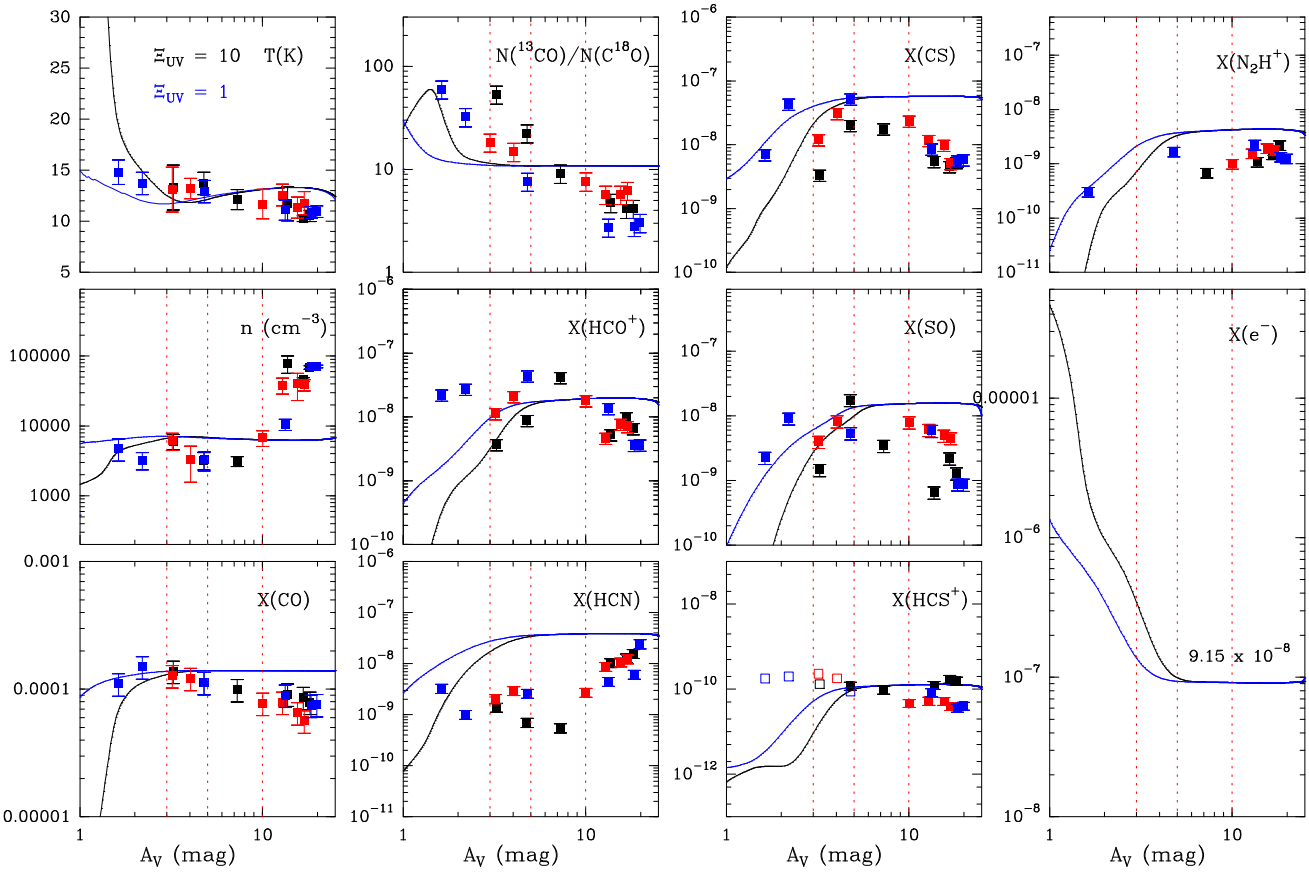

Fig. 9. Comparison between our "best-fit" model listed and the all the molecular abundances derived in this work. The black line corresponds to the side with χ_{UV}=10 and the blue line to χ_{UV}=1. The observational points are indicated with squares as in Fig 8.

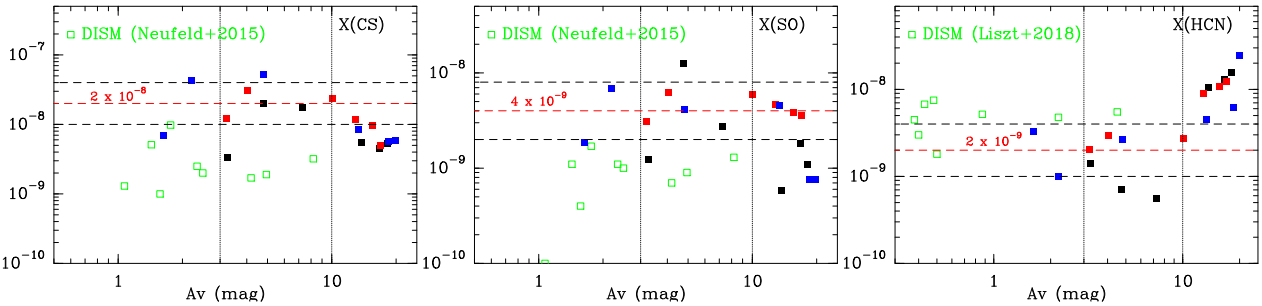

Fig. 10. Comparison between the abundances in TMC 1 with those observed in the diffuse gas by Neufeld et al. (2015) and Liszt et al. (2018).

for the observed abundances. We propose the scenario of two big depletion events in the depletion of S across the cloud, the first one in the transition between the diffuse and translucent phase where a large amount of S is expected to be in atomic form, and the second in the dense phase where the sulfur is expected to be mainly in molecular form, most likely as SO and SO_2. These molecules are rapidly frozen onto dust grains at high densities and temperature below ~50 K (see e.g. Pacheco-Vázquez et al., 2016), trapping the sulfur in the solid phase.

In Table 6 we compare our estimates with the sulfur depletion measured towards hot cores and bipolar outflows. In these regions, the icy mantles are destroyed and the sulfur budget trapped in the ice returns to the gas phase. Esplugues et al. (2014) needs to assume a sulfur depletion of ~10 to reproduce the observations towards the prototypical hot core Orion KL. A similar depletion was derived by Anderson et al. (2013) towards bipolar outflows using the observations of the infrared space telescope Spitzer. This depletion is similar to that we have estimated in the translucent phase. We propose that the 10% of the sulfur atoms thar are incorporated to the grain core in the diffuse phase, are not returned back to the gas phase during the star formation process.

12. Summary and conclusions

This paper is based on the (Gas phase Elemental abundances in Molecular CloudS, PI: A. Fuente) of the prototypical dark cloud TMC 1. The Taurus molecular cloud (TMC) is one of the closest, low-mass star forming regions at 140 pc.

– We use mm observations of a selected sample of species carried out with the IRAM 30m telescope (3mm and 2mm) and the 40m Yebes telescope (bands K and Q) to determine the fractional abundances of CO, HCO^+, HCN, CS, SO, HCS^+

Table 6 .- Elemental gas phase abundances

	Solar[1]	DIFF$_{min}$[2]	DIFF$_{max}$[3]	Translucent[4]	TMC 1-CP[5]	Orion KL[6]	Shocks[7]
C/H	2.88×10^{-4}	2.20×10^{-4}	1.76×10^{-4}	8.00×10^{-5}	4.00×10^{-5}	1.79×10^{-4}	1.79×10^{-4}
O/H	5.75×10^{-4}	5.50×10^{-4}	3.34×10^{-4}	8.00×10^{-5}	8.00×10^{-5}	4.45×10^{-4}	4.45×10^{-4}
S/H	1.50×10^{-5}	1.25×10^{-5}	3.50×10^{-6}	8.00×10^{-7}	$<8.00\times10^{-8}$	1.43×10^{-6}	6.00×10^{-7}

Ref:[1] Lodders et al. (2003); [2] Minimum depletion case of Jenkins (2009); [3]Maximum depletion case of Jenkins (2009); [4] Vidal et al. (2017); [5] Esplugues et al. (2014); [6] Holdship et al. (2016)

and N_2H^+ in positions along 3 cuts intersecting the main filament at positions TMC 1-CP, TMC 1-NH3 and TMC 1-C.

- None of the studied molecules present constant abundance across the studied cuts. According with their variations with visual extinction, we can differentiate three groups: i) the first group is formed by the most abundant molecule CO. This molecule reaches its peak value at $A_V\sim$ 3 mag and then progressively decreases with visual extinction; ii) the second group is formed by HCO^+, CS and SO; the abundances of these molecules increases with visual extinction until $A_V\sim$ 5 mag where they present a narrow peak and then progressively decreases towards the extinction peak; iii) The abundance of the N-bearing molecules HCN and N_2H^+ increases from $A_V\sim$3 mag until the extinctions peaks at $A_V\sim$20 mag.
- As a previous and imperative step to model the chemistry of TMC 1, we have estimate the incident UV field based on the visual extinction and dust temperature maps derived by Kirk et al. (2019, in prep). By using the expression of Hocuk et al. (2017) we derive χ_{UV} = 3−10 Drain e fields.
- By comparison the molecular abundances with the Meudon PDR code, we derive the C, O, and S depletions, and hence the gas ionization degree as a function of the visual extinction at each position. Our data show that even at A_V 3−4 mag where the transition C^+/C/CO occurs, significant depletions of C, O and S are found. In fact, C/H varies between $\sim8\ 10^{-5}$ to $\sim4\times10^{-5}$ in the traslucent cloud ($3 < A_V < 10$ mag). Moreover the C/O ratio is $\sim$ 1, suggesting that the O is preferentially depleted in the diffuse phase ($A_V < 3$ mag). Regarding sulfur, we estimate S/H $\sim 8\times10^{-7}$ in this moderate density region.

Based on our results, we propose that the freeze out of CO if the main process that changes the grain composition in the translucent part of the cloud producing a progressive depletion of C and O from $A_V\sim$ 3 mag to $A_V\sim$ 10. We do not have a clear hint of preferential depletion of O in this visual extinction range. Since C/O=1, we propose that O is preferentially depleted in the diffuse phase. Regarding sulfur, we measure a constant depletion of ∼20 across the translucent cloud. This suggests that sulfur atoms (or ions) would have been massively incorporated to dust grains from the HI/H_2 ($A_V\sim$1.5) to the CII/CI/CO transition ($A_V\sim$3 mag) to reach a depletion of ∼20 in the translucent medium. In order to account to the chemical composition in the TMC 1-CP core, a second big S depletion should occur in the dense cloud.

Acknowledgements. We thank the Spanish MINECO for funding support from AYA2016-75066-C2-1/2-P, and ERC under ERC-2013-SyG, G. A. 610256 NANOCOSMOS.

References

Agúndez, M. & Wakelam, V. 2013, Chemical Reviews, 113, 8710
Alonso-Albi, T., Fuente, A., Crimier, N., et al. 2010, A&A, 518, A52
Anderson, D. E., Bergin, E. A., Maret, S., & Wakelam, V. 2013, ApJ, 779, 141
André, P., Men'shchikov, A., Bontemps, S., et al. 2010, A&A, 518, L102
Bacmann, A., Lefloch, B., Ceccarelli, C., et al. 2002, A&A, 389, L6
Bernard, J.-P., Paradis, D., Marshall, D. J., et al. 2010, A&A, 518, L88
Bron, E., Daudon, C., Pety, J., et al. 2018, A&A, 610, A12
Cambrésy, L. 1999, A&A, 345, 965
Caselli, P., Walmsley, C. M., Tafalla, M., Dore, L., & Myers, P. C. 1999, ApJ, 523, L165
Caselli, P., Walmsley, C. M., Terzieva, R., & Herbst, E. 1998, ApJ, 499, 234
Caselli, P., Walmsley, C. M., Zucconi, A., et al. 2002, ApJ, 565, 344
Cernicharo, J. & Guelin, M. 1987, A&A, 176, 299
Dobashi, K., Shimoikura, T., Nakamura, F., et al. 2018, ArXiv e-prints
Dumouchel, F., Faure, A., & Lique, F. 2010, MNRAS, 406, 2488
Elias, J. H. 1978, ApJ, 224, 857
Esplugues, G. B., Viti, S., Goicoechea, J. R., & Cernicharo, J. 2014, A&A, 567, A95
Fehér, O., Tóth, L. V., Ward-Thompson, D., et al. 2016, A&A, 590, A75
Friesen, R. K., Pineda, J. E., co-PIs, et al. 2017, ApJ, 843, 63
Fuente, A., Cernicharo, J., Roueff, E., et al. 2016, A&A, 593, A94
Garrod, R. T. & Pauly, T. 2011, ApJ, 735, 15
Goldsmith, P. F., Heyer, M., Narayanan, G., et al. 2008, ApJ, 680, 428
Gratier, P., Majumdar, L., Ohishi, M., et al. 2016, ApJS, 225, 25
Griffin, M. J., Abergel, A., Abreu, A., et al. 2010, A&A, 518, L3
Hernandez, A. K., Tan, J. C., Caselli, P., et al. 2011, ApJ, 738, 11
Hocuk, S., Szűcs, L., Caselli, P., et al. 2017, A&A, 604, A58
Hollenbach, D. J., Takahashi, T., & Tielens, A. G. G. M. 1991, ApJ, 377, 192
Jenkins, E. B. 2009, ApJ, 700, 1299
Kirk, J. M., Ward-Thompson, D., Palmeirim, P., et al. 2013, MNRAS, 432, 1424
Kramer, C., Alves, J., Lada, C. J., et al. 1999, A&A, 342, 257
Lippok, N., Launhardt, R., Semenov, D., et al. 2013, A&A, 560, A41
Lique, F., Cernicharo, J., & Cox, P. 2006a, ApJ, 653, 1342
Lique, F., Cernicharo, J., & Cox, P. 2006b, ApJ, 653, 1342
Liszt, H., Gerin, M., Beasley, A., & Pety, J. 2018, ApJ, 856, 151
Liszt, H. & Lucas, R. 1996, A&A, 314, 917
Liszt, H. & Lucas, R. 2001, A&A, 370, 576
Loison, J.-C., Wakelam, V., & Hickson, K. M. 2014, MNRAS, 443, 398
Lucas, R. & Liszt, H. 1998, A&A, 337, 246
Malinen, J., Juvela, M., Rawlings, M. G., et al. 2012, A&A, 544, A50
Maret, S., Bergin, E. A., & Tafalla, M. 2013, A&A, 559, A53
McKee, C. F. 1989, ApJ, 345, 782
Miettinen, O. & Offner, S. S. R. 2013, A&A, 555, A41
Mizuno, A., Onishi, T., Yonekura, Y., et al. 1995, ApJ, 445, L161
Narayanan, G., Heyer, M. H., Brunt, C., et al. 2008, ApJS, 177, 341
Neufeld, D. A., Godard, B., Gerin, M., et al. 2015, A&A, 577, A49
Ohishi, M. & Kaifu, N. 1998, Faraday Discussions, 109, 205
Onishi, T., Mizuno, A., Kawamura, A., Ogawa, H., & Fukui, Y. 1996, ApJ, 465, 815
Onishi, T., Mizuno, A., Kawamura, A., Tachihara, K., & Fukui, Y. 2002, ApJ, 575, 950
Pacheco-Vázquez, S., Fuente, A., Baruteau, C., et al. 2016, A&A, 589, A60
Padoan, P., Cambrésy, L., & Langer, W. 2002, ApJ, 580, L57
Padovani, M., Galli, D., & Glassgold, A. E. 2009, A&A, 501, 619
Padovani, M., Hennebelle, P., & Galli, D. 2013, A&A, 560, A114
Poglitsch, A., Waelkens, C., Geis, N., et al. 2010, A&A, 518, L2
Savage, B. D. & Sembach, K. R. 1996, ARA&A, 34, 279
Schnee, S., Caselli, P., Goodman, A., et al. 2007, ApJ, 671, 1839
Schnee, S., Enoch, M., Noriega-Crespo, A., et al. 2010, ApJ, 708, 127
Ungerechts, H. & Thaddeus, P. 1987, ApJS, 63, 645
van der Tak, F. F. S., Black, J. H., Schöier, F. L., Jansen, D. J., & van Dishoeck, E. F. 2007, A&A, 468, 627
Vidal, T. H. G., Loison, J.-C., Jaziri, A. Y., et al. 2017, MNRAS, 469, 435
Zhao, B., Caselli, P., Li, Z.-Y., et al. 2016, MNRAS, 460, 2050
Zucconi, A., Walmsley, C. M., & Galli, D. 2001, A&A, 376, 650

Appendix A: Tables and Figures

Table A.1- Telescope parameters

Telescope	Setup	Freq. band	HPBW(")	F_{ff}	B_{eff}
IRAM 30m	Setup 1	L106	24	0.95	0.80
	Setup 2	L89	29	0.95	0.81
		L147	16	0.93	0.74
	Setup 3	L101	25	0.95	0.80
		L138	17	0.93	0.74
	Setup 4	L92	17	0.95	0.81
		L168	14	0.93	0.74
				T_{mb}/T_a^*	$S(Jy)/T_{mb}(K)$
Yebes 40m	Setup 0	L23000	84	1.3	4.1
		L44750	42	2.1	4.8

Table A.2 .- Spectral setups

Line		Freq.(MHz)	E_u(K)	A_{ul}(s^{-1})	g_u
		L89			
HCS^+	2→1	85347.87	6.1	$1.110\ 10^{-5}$	5
HCN	1→0	88631.85	4.3	$2.406\ 10^{-5}$	3
$H^{13}CN$	1→0	86339.92	4.1	$2.224\ 10^{-5}$	3
$HC^{15}N$	1→0	86054.97	4.1	$2.202\ 10^{-5}$	3
HCO^+	1→0	89188.53	4.3	$4.234\ 10^{-5}$	3
$H^{13}CO^+$	1→0	86754.29	4.2	$3.897\ 10^{-5}$	3
$HC^{18}O^+$	1→0	85162.22	4.1	$3.686\ 10^{-5}$	3
HNC	1→0	90663.56	4.4	$2.690\ 10^{-5}$	3
OCS	7→6	85139.10	16.3	$1.715\ 10^{-6}$	15
SO	2_2→1_1	86093.96	19.3	$5.250\ 10^{-6}$	5
		L92			
^{13}CS	2→1	92494.27	6.7	$1.412\ 10^{-5}$	5
$C^{34}S$	2→1	96412.95	6.9	$1.600\ 10^{-5}$	5
CH_3OH	2,-1→1,-1	96739.36	4.6	$2.558\ 10^{-5}$	5
CH_3OH	2,1→1,1	96741.37	7.0	$3.408\ 10^{-6}$	5
		L101			
CS	2→1	97980.95	7.1	$1.679\ 10^{-5}$	5
SO	2_3→1_2	99299.89	9.2	$1.125\ 10^{-5}$	7
^{34}SO	2_3→1_2	97715.40	9.1	$1.073\ 10^{-5}$	7
H_2CS	3(1,2)→2(1,2)	101477.81	8.1	$1.260\ 10^{-5}$	7
		L106			
13CO	1→0	110201.35	5.3	$6.336\ 10^{-8}$	3
$C^{18}O$	1→0	109782.17	5.3	$6.263\ 10^{-8}$	3
N_2H^+	1→0	93173.77	4.5	$3.628\ 10^{-5}$	3
SO	3_2→2_1	109252.18	21.1	$1.080\ 10^{-5}$	5
^{34}SO	3_2→2_1	106743.37	20.9	$1.007\ 10^{-5}$	5
NH_2D	1(1,1)→1(0,1)	110153.59	21.3	$5.501\ 10^{-6}$	9
CH_3OH	0,0→1,-1	108893.94	5.2	$1.471\ 10^{-5}$	3
		L138			
^{13}CS	3→2	138739.26	13.3	$5.107\ 10^{-05}$	7
SO	3_4→2_3	138178.66	15.9	$3.166\ 10^{-05}$	9
OCS	11→10	133785.90	38.5	$6.818\ 10^{-06}$	23
H_2CS	4(0,4)→3(0,3)	137371.21	16.5	$3.647\ 10^{-05}$	9
HDCO	2(1,1)→1(1,0)	134284.90	17.6	$4.591\ 10^{-05}$	5
		L147			
CS	3→2	146969.03	14.1	$6.071\ 10^{-05}$	7
$C^{34}S$	3→2	144617.10	13.9	$5.784\ 10^{-05}$	7
		L168			
H_2S	1(1,0)→1(0,1)	168762.75	8.1	$2.677\ 10^{-05}$	3
$HH^{34}S$	1(1,0)→1(0,1)	167910.52	8.1	$2.616\ 10^{-05}$	3
HCS^+	4→3	170691.62	20.5	$9.863\ 10^{-05}$	9
$HC^{34}S^+$	4→3	167927.25	20.1	$7.805\ 10^{-05}$	9
SO	4_4→3_3	172181.42	33.8	$5.833\ 10^{-05}$	9
^{34}SO	4_4→3_3	168815.11	33.4	$5.498\ 10^{-05}$	9
		L23000			
NH_3	(1,1)a→(1,1)s	23694.49	1.1	$1.712\ 10^{-07}$	12
NH_3	(2,2)a→(2,2)s	23722.63	42.3	$2.291\ 10^{-07}$	20
		L44500			
CS	1→0	48990.96	2.4	$1.749\ 10^{-06}$	3
$C^{34}S$	1→0	48206.94	2.3	$1.666\ 10^{-06}$	3
^{13}CS	1→0	46247.56	2.2	$1.471\ 10^{-06}$	3
HCS^+	1→0	42674.19	2.0	$1.156\ 10^{-06}$	3
OCS	4→3	48651.60	5.8	$3.047\ 10^{-07}$	9

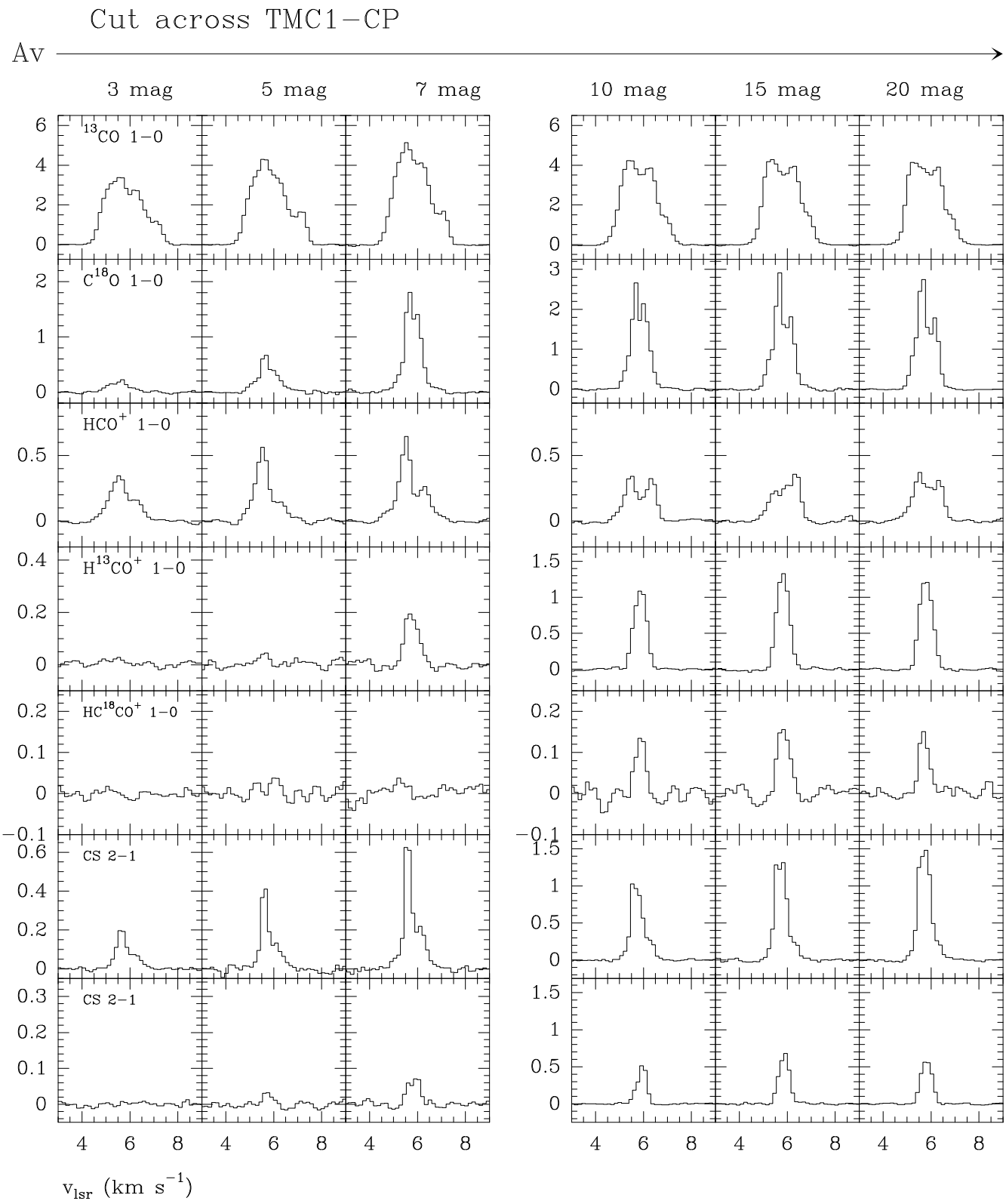

Fig. A.1. Selected sample of spectra as observed with the 30m telescope towards the TMC 1-CP cut.

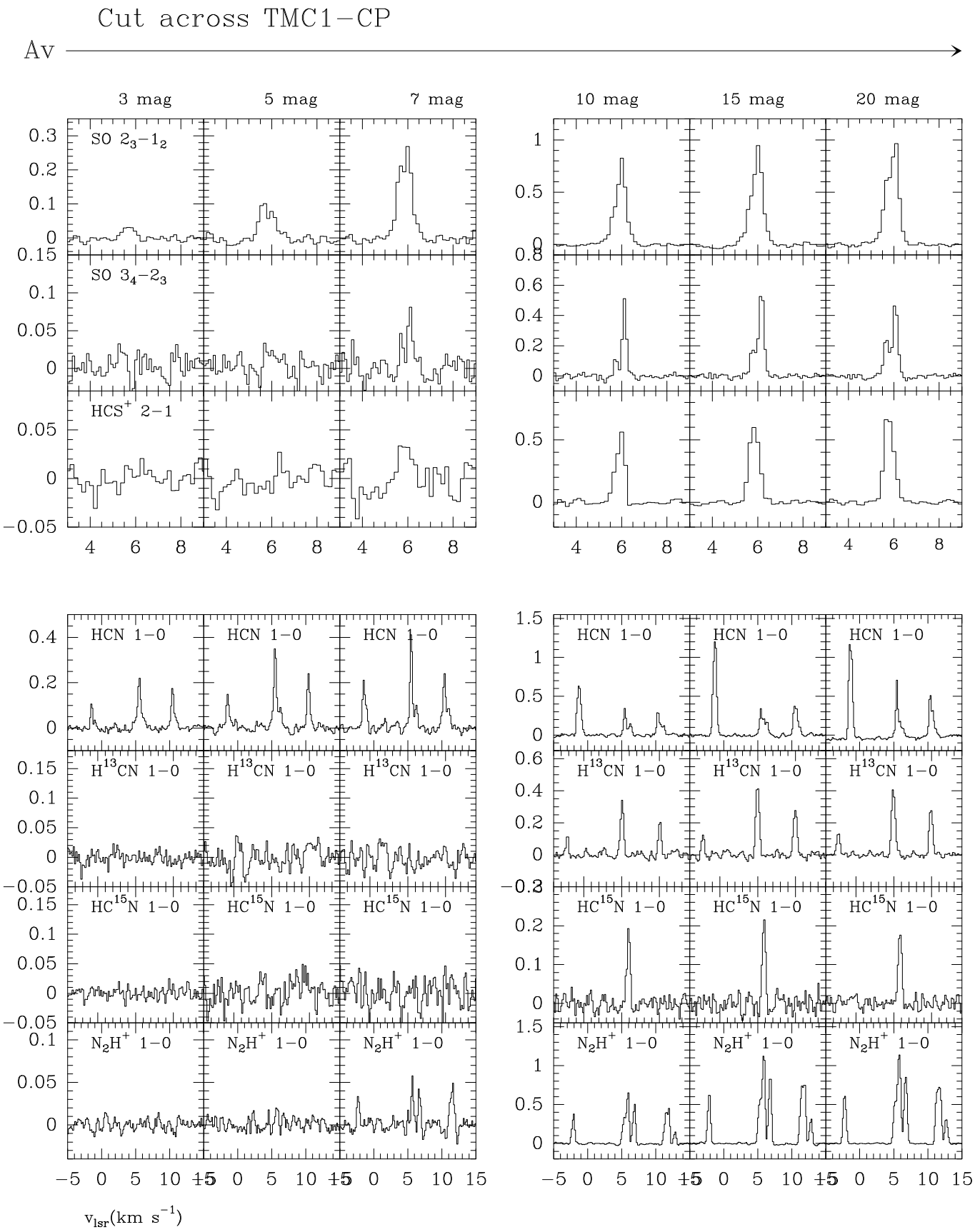

Fig. A.2. The same as Fig. A.1

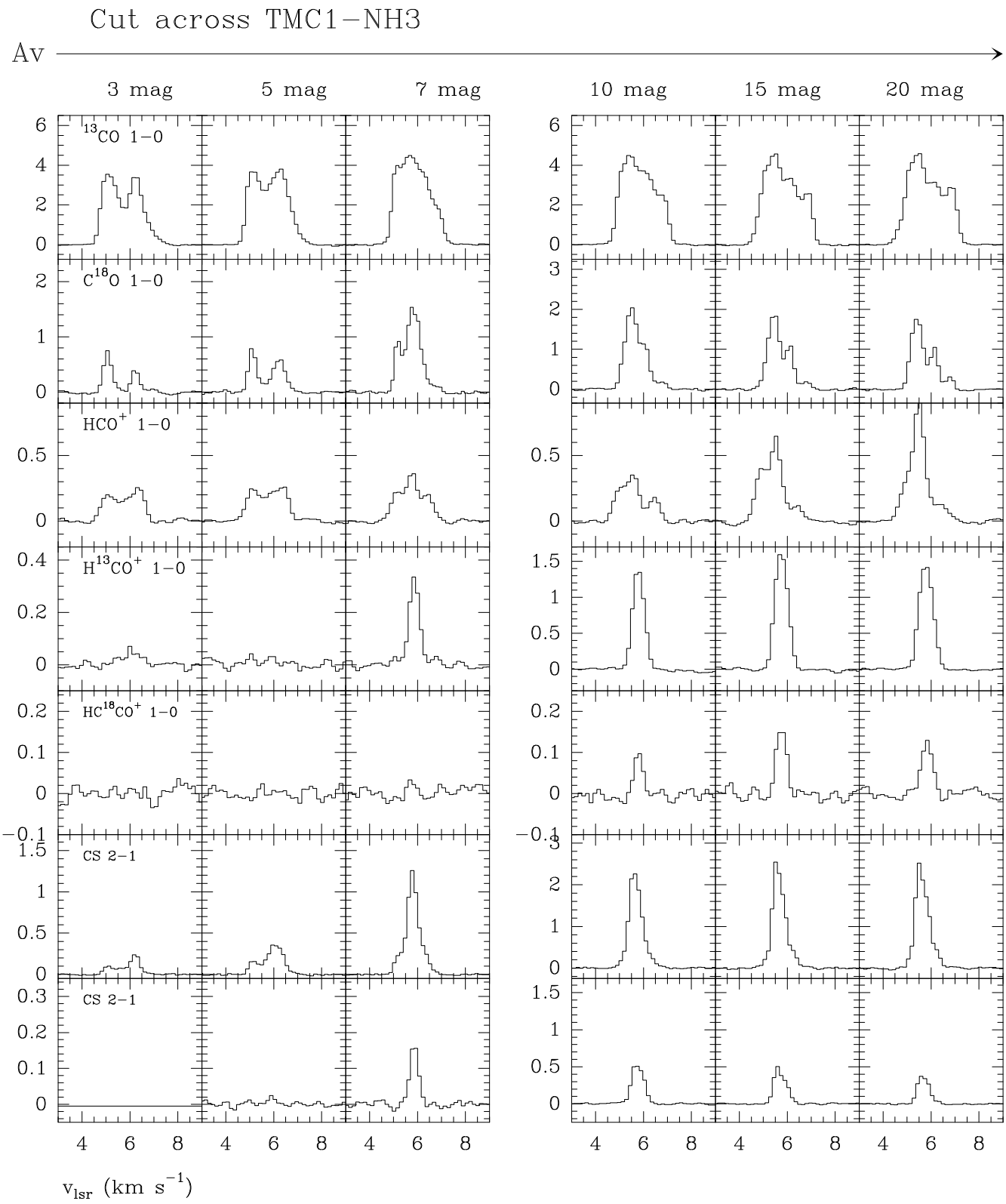

Fig. A.3. Selected sample of spectra as observed with the 30m telescope towards the TMC 1-NH3 cut.

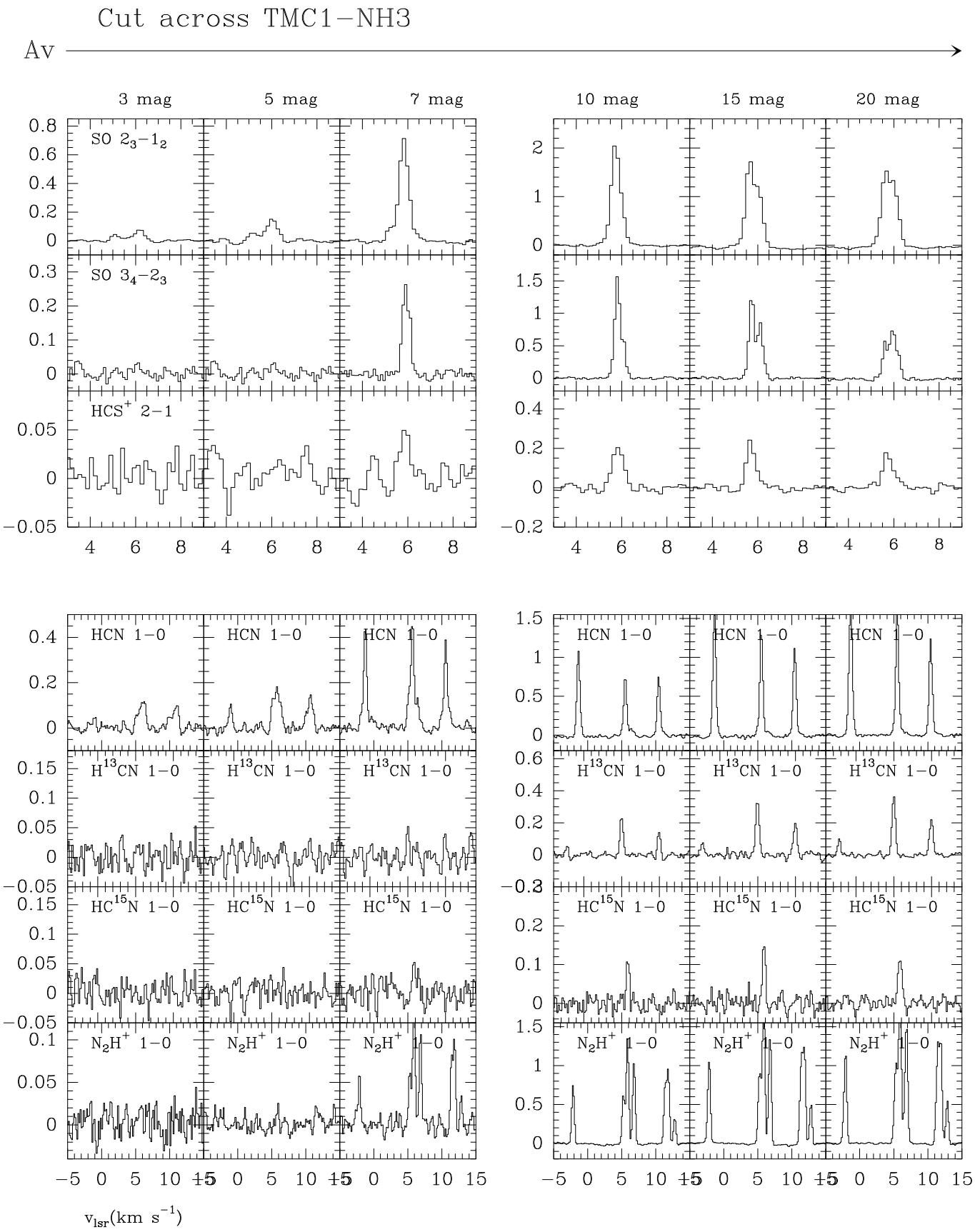

Fig. A.4. The same as Fig. A.3

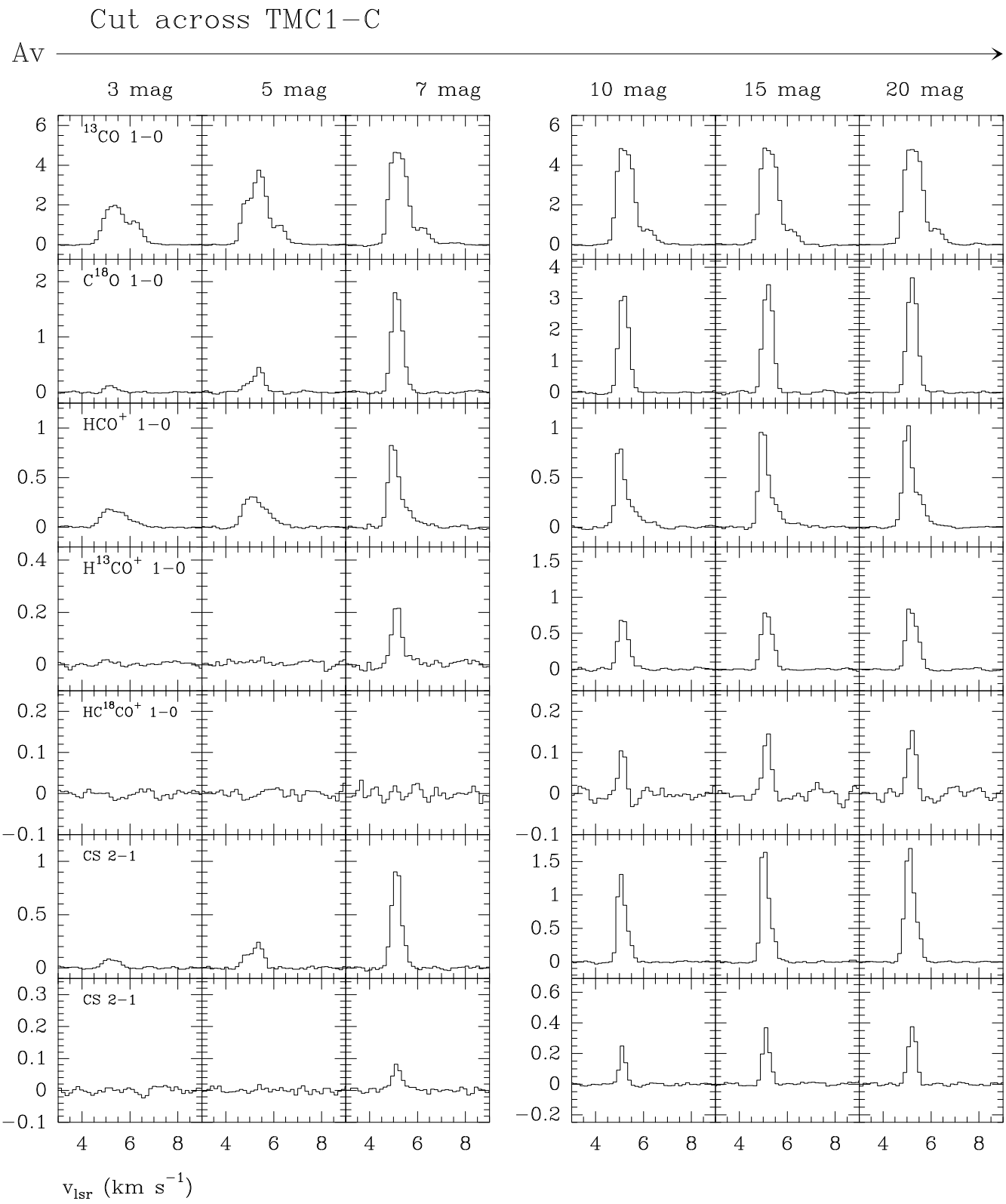

Fig. A.5. Selected sample of spectra as observed with the 30m telescope towards the TMC 1-NH3 cut.

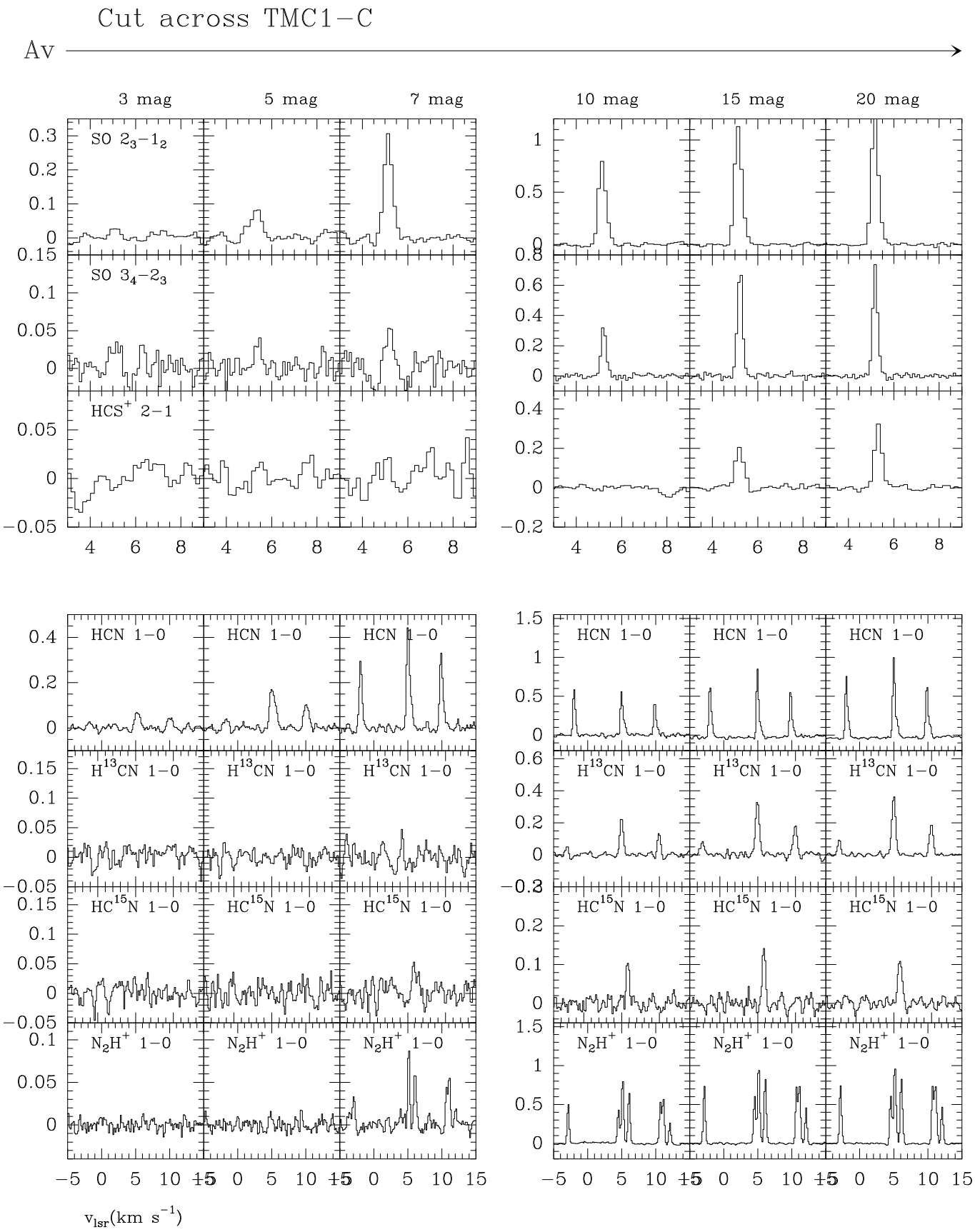

Fig. A.6. The same as Fig. A.5